Structure, phase evolution and mechanical properties of HiPIMS, pulsed DC and DC sputtered Ta-N films

Diploma Thesis

by

Heribert Marihart

Christian Doppler Laboratory for Application Oriented Coating

Development at the Institute of Materials Science and Technology,

Vienna University of Technology

Vienna, March 2015

This work was supported by Plansee Composite Materials GmbH and
Oerlikon Surface Solutions AG in the framework of the Christian Doppler Laboratory
for Application Oriented Coating Development.

Affidavit:
I declare in lieu of oath, that I wrote this thesis and performed the associated research myself, using only literature cited in this volume.

Date *Signature*

Acknowledgements

First of all, I want to thank my supervisor **Univ.-Prof. DI Dr. mont. Paul Heinz Mayrhofer** for giving me the opportunity of writing my Master thesis in his dedicated Thin Film Group within the framework of the Christian Doppler Laboratory for Application Oriented Coating Development. I have been a member of Pauls group ever since I first applied for a student assistant position in Leoben. In his natural way he was always open for scientific and probably more often non-work-related discussions during our frequent coffee breaks. Being part of this group led by an extraordinary person was an exceptional honor to me, and it was a time I will always keep in good memory. Moreover, he made it possible for me to attend a highly educational research stay at Colorado School of Mines in USA. Thank you very much for your sympathetic and positive support.

I am especially grateful to **Christian Koller** as my advisor, for his continuous help and guidance. He supported me gratefully and discussed my results and issues with me in Vienna or Leoben. I am outstandingly thankful for his valuable time and patience.

I am also grateful to my longstanding colleagues **Helmut Riedl** and **Robert Hollerweger** for enrolling on the deposition facility Ilvy and for their assistance and advice concerning practical aspects of the investigated material system. Appreciation deserves also the entire Thin Film Group.

Last but not least, a sincere thanks to **my family** for their necessary support and for enabling me to study, and also many thanks to my sweetheart **Claudia**. She always gave me the energy to do my work with joy and she motivated and stood beside me in good and hard times.

Contents

Contents **iv**

List of Figures **vi**

Abstract **1**

1 Introduction **3**

2 Deposition techniques **5**

2.1 Physical vapor deposition . . . 5

2.2 Plasma discharge . . . 6

2.3 Sputtering . . . 9

2.3.1 DC sputtering . . . 11

2.3.2 Pulsed DC sputtering . . . 12

2.3.3 High power impulse magnetron sputtering . . . 13

2.4 Thin film growth . . . 14

2.4.1 Basics of nucleation and grain growth . . . 14

2.4.2 Structure zone model . . . 15

3 Coating systems **18**

3.1 Ta . . . 19

3.2 TaN . . . 19

4 Characterization techniques **21**

4.1 Coating thickness measurement 21

4.2 X-ray diffraction 22

4.3 Nanoindentation 25

4.4 Scanning electron microscopy 26

Bibliography **28**

Publication I **32**

List of Figures

2.1 Classification of PVD 6
2.2 Plasma sheath: a) potential versus distance, b) particle density versus distance . 7
2.3 a) basics of sputter deposition, adapted after Martin, b) structure of a glow discharge 8
2.4 Schematic plasma voltage-currant characteristic 9
2.5 Unbalanced magnetron sputtering 11
2.6 Schematic voltage characteristic of pulsed DC sputtering 12
2.7 Target voltage and current waveforms during a long-pulse operation 13
2.8 a) Layer-by-layer growth, b) 3D island growth, and c) mixed growth 14
2.9 Schematic representation of various strucutre zones 16
2.10 Extended structure zone model by Anders 17

3.1 Hard ceramic-like coatings classified in terms of bonding character and mechanical properties 18
3.2 a) bcc Ta structure, b) tetragonal Ta structure 19
3.3 TaN 20

4.1 Schematic of a ball-crater-test 21
4.2 a) Bragg-Brentano arrangement, b) grazing incidence arrangement, c) schematic arrangement of Bragg's diffraction 23
4.3 Schematic XRD pattern a) peak position, b) peak shift, c) peak height, and d) peak width (FWHM) 24
4.4 Schematic diagram of a load-displacement curve 25
4.5 Interaction of the electron beam with the sample and corresponding information of generation depth out of the specimen used for materials characterization . . . 26
4.6 Generation of characteristic X-rays and secundary electrons based on the impact of accelerated electrons 27

Abstract

Abstract

The microstructural development of reactively sputtered tantalum nitride thin films is investigated as a function of the N_2-to-total pressure ratio (p_{N2}/p_T) and the operating mode of the metallic tantalum cathode by high power impulse magnetron sputtering (HiPIMS), pulsed direct current (DC) and DC sputtering.

For all sputtering modes investigated, the phase evolution of the Ta-N films strongly depends on the nitrogen partial pressure, p_{N2}, used when keeping the total pressure, p_T, constant at 0.3 or 0.6 Pa. The major crystalline phases identified, with increasing the N_2-to-total pressure ratio, are α- and β-Ta, orthorhombic o-Ta_4N, hexagonal close packed (hcp γ-Ta_2N, cubic δ-TaN, and hcp ϵ-TaN, respectively. The minimum p_{N2}/p_T-ratio needed for the formation of the individual nitride phases, decreases from DC to HiPIMS. For example, when using a p_{N2}/p_T-ratio of 13.4%, the nitrogen content within the HiPIMS film is $\approx$ 38.5 at.%, but only $\approx$ 26.5 at.% within the pulsed DC and DC sputtered films. Therefore, the HiPIMS film is mainly composed of γ-Ta_2N (with traces of ϵ-TaN) whereas the pulsed DC and DC sputtered films also contain o-Ta_4N next to γ-Ta_2N. These coatings—with a majority of γ-TaN—exhibit the highest hardness values with 38.2 ± 4.6, 38 ± 2.3, and 40 ± 3.8 GPa among all samples studied, respectively. Further increasing p_{N2}/p_T leads to the formation of δ- and ϵ-TaN, which are the dominating phases for p_{N2}/p_T-values above 38.1%. For higher N_2-to-total pressure ratios, the phase fraction of ϵ-TaN increases on the expanse of δ-TaN and a significant reduction in hardness, even down to $\approx$ 20 GPa, is observed.

Based on our results we can conclude that the highest hardness is obtained for γ-Ta_2N dominated films. Consequently, with respect to mechanical properties, the most important p_{N2}/p_T range is between 13.4 and 38.1%, where the films undergo a transformation from γ-Ta_2N (plus o-Ta_4N) to δ- and ϵ-TaN. Generally, this phase transformation is shifted to lower p_{N2}/p_T-values when using HiPIMS instead of pulsed DC or DC sputtering.

Kurzfassung

Der mikrostrukturelle Schichtaufbau von reaktive abgeschiedenen Tantal-Nitrid Schichten ist in Abhängigkeit von Stickstoffpartialdruck und Betriebsart der metallischen Tantalkathode mit high power impulse magnetron sputtering (HiPIMS), gepulstem Gleichstrom oder Gleichtrom sputtern (pulsed DC, DC) untersucht worden.

Die Phasenentwicklung von Ta-N Dünnschichten wurde abhängig von den verwendeten Stickstoffpartialdrücken, p_{N2}, bei konstantem Gesamtdruck, p_T, von 0.3 or 0.6 Pa, für alle Abscheidungstechniken untersucht. Die wesentlichsten kristallinen Phasen, die identifiziert werden konnten, sind α- und β-Ta, orthorhomisches o-Ta_4N, hcp γ-Ta_2N, sowie kubisches δ- und hcp ϵ-TaN. Das minimale Verhältnis von Stickstoff- zu Gesamtdruck, p_{N2}/p_T, welches für die Bildung der jeweiligen Nitridphase notwendig ist, nimmt von DC Sputtern zu HiPIMS ab. Dies beruht hauptsächlich auf der wesentlich höheren Teilchen-Reaktivität beim HiPIMS Prozess. Bei einem Stickstoffpartialdruck von 13.4% des Gesamtdrucks, weisen HiPIMS Schichten einen Stickstoffgehalt von ≈ 38.5 at.% auf, wohingegen Schichten, die mit pulsed DC oder DC Sputtern hergestellt wurden, nur ≈ 26.5 at.% N enthalten. Deshalb besteht der überwiegende—Anteil von HiPIMS Dünnschichten aus γ-Ta_2N (mit Anteilen von ϵ-TaN), wobei gepulst DC und DC gesputterte Schichten neben γ-Ta_2N auch noch Ta-reiches, orthorhombisches o-Ta_4N enthalten. Diese Schichten, mit derartiger Phasenzusammensetzung, weisen die höchsten Härtewerte von allen untersuchten Proben auf (38.2 ± 4.6, 38 ± 2.3, und 40 ± 3.8 GPa). Ein weiterer Anstieg des Stickstoffpartialdrucks führt zur Bildung der Phasen δ- und ϵ-TaN, welche im Allgemeinen für p_{N2}/p_T-Werte über 38.1% dominieren. Bei noch höheren Verhältnis von Stickstoff- zu Gesamtdruck nimmt der Phasenanteil von ϵ-TaN auf Kosten der δ-Phase zu, dadurch wird auch eine signifikante Abnahme der Härte bis zu ≈ 20 GPa beobachtet.

Zusammenfassend können wir aufgrund unserer Untersuchungsergebnisse festhalten, dass γ-Ta_2N dominierte Hartstoffschichten die höchsten Härte- und E-Modul-Werte aufweisen. Folglich ist in Bezug auf mechanische Eigenschaften der p_{N2}/p_T Bereich zwischen 13.4 und 38.1% von groer Bedeutung, da hier die Phasenumwandlung von γ-Ta_2N (sowie o-Ta_4N) zu δ- und ϵ-TaN stattfindet. Bei HiPIMS wird diese Phasenumwandlung bereits bei geringeren p_{N2}/p_T-Werten erhalten als bei gepulst DC oder DC gesputterten Schichten.

Chapter 1

Introduction

Materials science and engineering have become strongly connected to each other, both aiming for enhanced performance and durability of technical components and tools. High hardness, good wear and corrosion resistance, and high thermal stability are essential properties of cutting inserts or forming tools. Bulk materials are quite often not capable meeting these requirements, which gives rise to the application of surface modification treatments. One of the most prominent methods is the deposition of a thin functional coating by physical vapor deposition (PVD). Nitride-based materials, such as transition metal nitrides, have proven to be extremely efficient for forming, cutting, or milling applications [1–6].

Reactive sputter deposition (RSD), and High Power Impulse Magnetron Sputtering (HiPIMS) are among the most important and manifold PVD technologies available. Alloying concepts and the improvement of deposition techniques are within the focus of current research, as both of them allow for modifications of the coatings microstructure, synonymously for fine-tuning of properties and performance during application [5–8].

Tantalum nitride thin films are well established in the microelectronic industry. For example, they are used as thin film resistors and diffusion barriers [9–14]. Recent studies also attribute excellent mechanical properties to tantalum nitride coatings [9, 12, 14–17]. However, the tantalum-nitride system for PVD processed coatings is quite complex and features a large number of different crystallographic phases, as for instance α-Ta(N), hexagonal-close-packed (hcp) γ-Ta_2N (ϵ-Fe_2N-prototype), hcp ϵ-TaN, body-centered cubic (bcc) β-Ta(N), hexagonal (hex) Ta_2N, hex θ-TaN (WC-prototype), cubic B1 δ-TaN (NaCl-prototype), hex Ta_5N_6 (Nb_5N_6-type), tetragonal Ta_4N_5, and orthorhombic Ta_3N_5 [9, 12, 14, 15, 18–21]. Consequently, a large number of different properties are to be expected. In turn, experimentalists have to carefully adjust deposition conditions in order to grow Ta-N films with the desired microstructure and properties.

For this reason, the present work is focused on the comparison of three different PVD tech-

nologies, HiPIMS, pulsed DC and direct current (DC) sputtering. This paper investigates and discusses the microstructure and resulting mechanical properties of Ta-N thin films as a function of the nitrogen partial pressure (ranging from 0 to 100%), and the deposition technology.

Chapter 2

Deposition techniques

2.1 Physical vapor deposition

Physical vapor deposition is nowadays an important and widely used method to improve the surface properties of technical components and tools [22, 23]. The main advantage over other industrially utilized deposition techniques, as for instance chemical vapor deposition (CVD), is the large number of accessible target materials and the possibility to grow films at significantly reduced deposition temperatures without the necessity of precursors and chemical reactions to transfer the target material into gaseous state. Furthermore, the substrate material may significantly suffer from typical CVD process temperatures, which is in the range of 800 to 1200 C [6, 23].

PVD can be described by three main processes: [5]:

- evaporation of the solid target material by physical means exclusively
- transfer of the vaporized target material to the substrate
- condensation of the vapor phase, nucleation, and film growth

A general classification of PVD methods includes three basic sub-technologies: sputter deposition, evaporation, and ion plating as illustrated in Fig. 2.1. Sputter deposition is based on momentum transfer of ionized particles which arise from a plasma discharge. Evaporation is achieved by thermal energy input, whereas ion plating can be seen as a combination of sputtering and evaporation. [24]. Methods used in this work are highlighted.

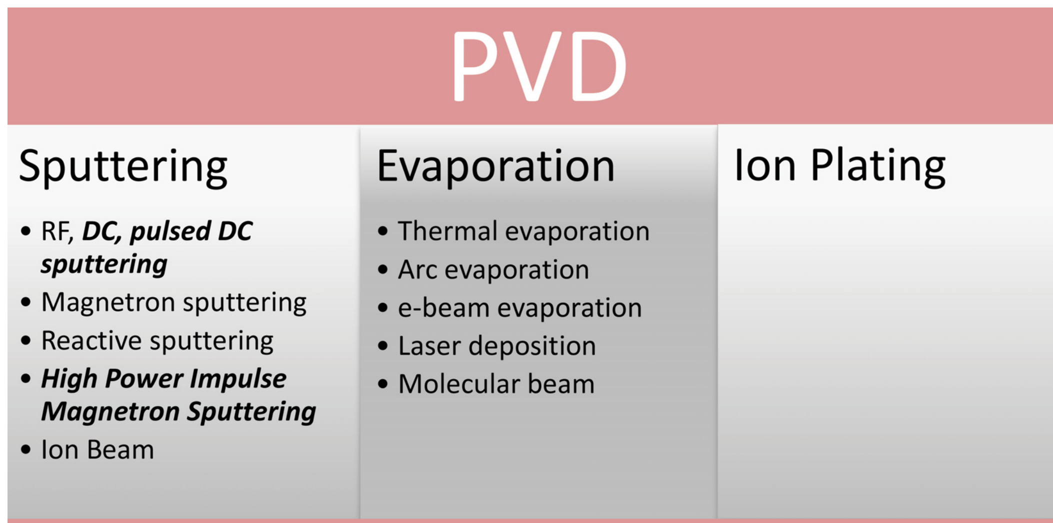

Figure 2.1: Classification of PVD [24].

2.2 Plasma discharge

The fundamental process of sputter deposition is the evaporation of a solid target material by momentum transfer of impinged charged particles. These particles are generated from an inert working gas, typically Argon. When an electron and an Ar atom with sufficient high kinetic energy collide, the Ar atom will be ionized with the result of an excited electron, according to equation 2.1.

$$e^- + Ar = Ar^+ + 2e^- \quad (2.1)$$

Consequently, each collision represents a source for further electrons. This cascade-like process continuously increases the number of involved particles. However, in this dynamic process electrons and Ar ions may also recombine. In this arrangement of sputter deposition the target is defined as cathode and the substrate as anode. Due to the potential difference between cathode and anode, the positive charged ions are accelerated towards the target surface. Impinging ions kick out metal atoms which then leave the target surface under a certain angular distribution. The probability of further collisions with Ar^+ ions and electrons is given. However, most of the ejected particles will pass the target near area of high plasma density and migrate to the chamber walls and substrate that is located opposite of the target area, where film growth occurs.

The essential component of every sputter process is the plasma. It is typically referred to as quasi-neutral state of matter with collective behavior. The term quasi-neutral state indicates that all load carriers cancel out when observing this process from outside [25]. Collective behavior can be understood as the response of plasma species not only to local forces (i.e. at the very vicinity of particles), but also on non-local forces [26]. Plasma consists of negative charge carriers (i.e. electrons), ions, and atoms or clusters of atoms. A

stable plasma is usually separated in different areas which exhibit fundamentally different properties and characteristics. The quantity of electrons and ions inside the bulk plasma is in equilibrium, Fig. 2.2b. Electrons, which have a higher mobility than ions, consequentially also have a higher probability to leave the bulk plasma via the chamber walls. Therefore, the ratio of electrons and ions deviates from the ideal balanced with decreasing distance to the chamber walls. The same applies for all other objects which are in contact with the plasma, e.g. grounded electrodes. At the very beginning, both ions and electrons decrease equally. This region is called pre-sheath. In the adjacent area the number of electrons then rapidly decreases. In order to establish a stable plasma, the pre-sheath and sheath have to be small in relation to the bulk plasma. The sheath expansion strongly correlates with the plasma properties and is usually a few Debye lengths (scale, in which the electrostatic charge carrier effects appear), λ_D, large (see Fig. 2.2a). Depending on the current density passing across the sheath, a sheath potential develops, which acts as a barrier to electrons. The positively charged sheath space is also referred to as ion sheath. This ion sheath is self-adjusting, thereby the electron flux towards the wall is equal to the electron flux supplied by an external circuit. In case of an electrically isolated wall the situation is slightly different. The electron flux is reduced until an equilibrium with the ion flux is present. The potential—in respect to the plasma potential—is referred to as floating potential, V_f. Typical values are in the range of 5-50 V. The plasma sheath potential, V_s, obeys to the Child-Langmuir law, whereas the pre-sheath plasma potential, V_{ps}, is related to the presheath and can be represented by a Boltzmann distribution. This is illustrated in Fig. 2.2a [5].

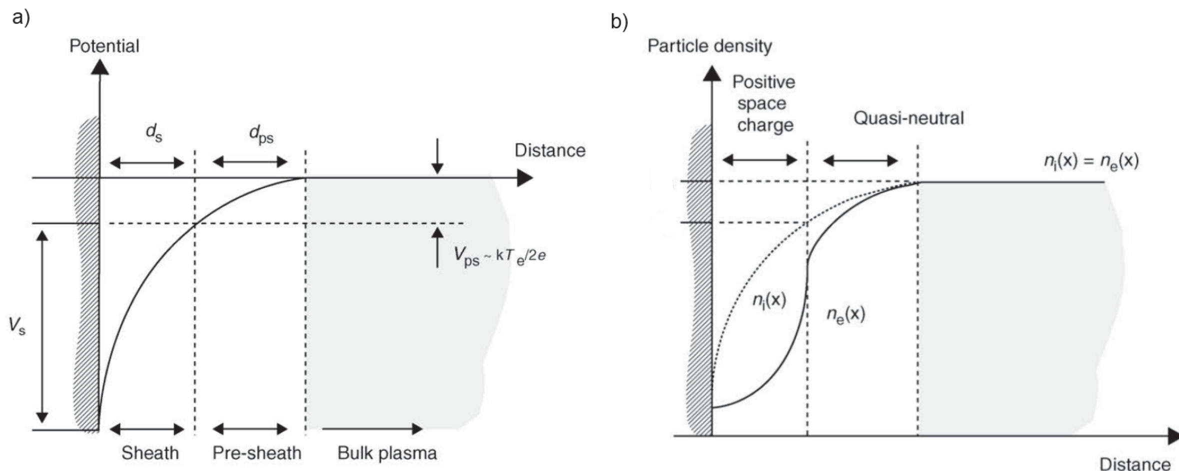

Figure 2.2: Plasma sheath: a) potential versus distance, b) particle density versus distance [5].

A representative sputter arrangement is represented in Fig. 2.3a. Two electrodes are oppositely located in a vacuum chamber. The plasma is ignited by the application of a high voltage difference between a cathode (source material) and an anode (chamber walls, sub-

strate). In order to ignite a plasma, the working gas (in this case Ar) is injected into the chamber. Three different zones of plasma discharges can be distinguished, which feature different current-voltage characteristics (Fig. 2.4), and mainly depend on the geometry of the electrodes and chamber, the cathode material as well as the (reactive and working) gas conditions used.

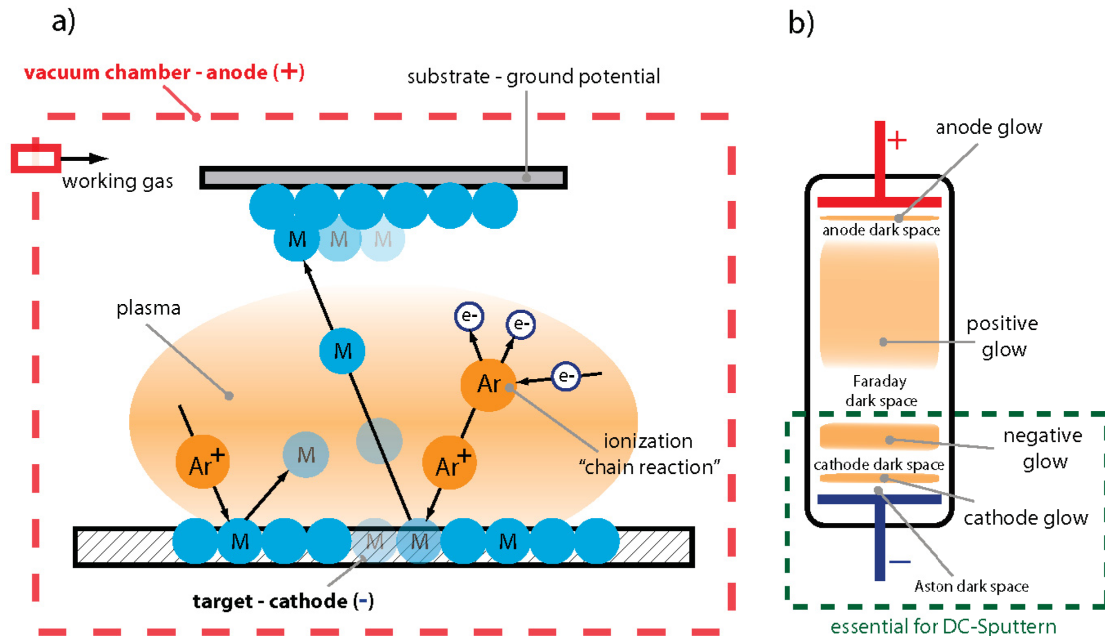

Figure 2.3: a) basics of sputter deposition, adapted after Martin [27], b) structure of a glow discharge [5].

The very beginning (if no voltage is applied) represents the dark discharge area, in which only a small fraction of load carries is available arising from background ionization (A in Fig. 2.4). By applying a voltage the amount of ions is increased, hence a current increase is detectable until the system reaches a steady-state (B in Fig. 2.4). The current remains constant, whereas all ions are attracted to the electrodes. If a sufficiently high voltage is present, the current saturates. With a further voltage increase electrons, located in the large anode area, gain enough energy (point C) to trigger a chain reaction of impact ionization with ambient working gas atoms. At this stage, all generated ions and electrons arrive at the electrodes. Characteristic for this townsend discharge region is a rapid current increase. A self-preserving plasma is established. At the breakdown voltage (point E in Fig. 2.4), the current steadily increases, whereas the voltage is self regulated to a certain value by the electrical field of the internal resistance of the power supply. As a consequence of the increasing power the plasma, hence ion bombardment, extends over the entire cathode surface. This stage is called glow discharge, depicted in Fig. 2.3b, and visible with the naked eye. For the sputter technique used, the dark layers (established Aston dark space, cathode glow, and cathode dark space)

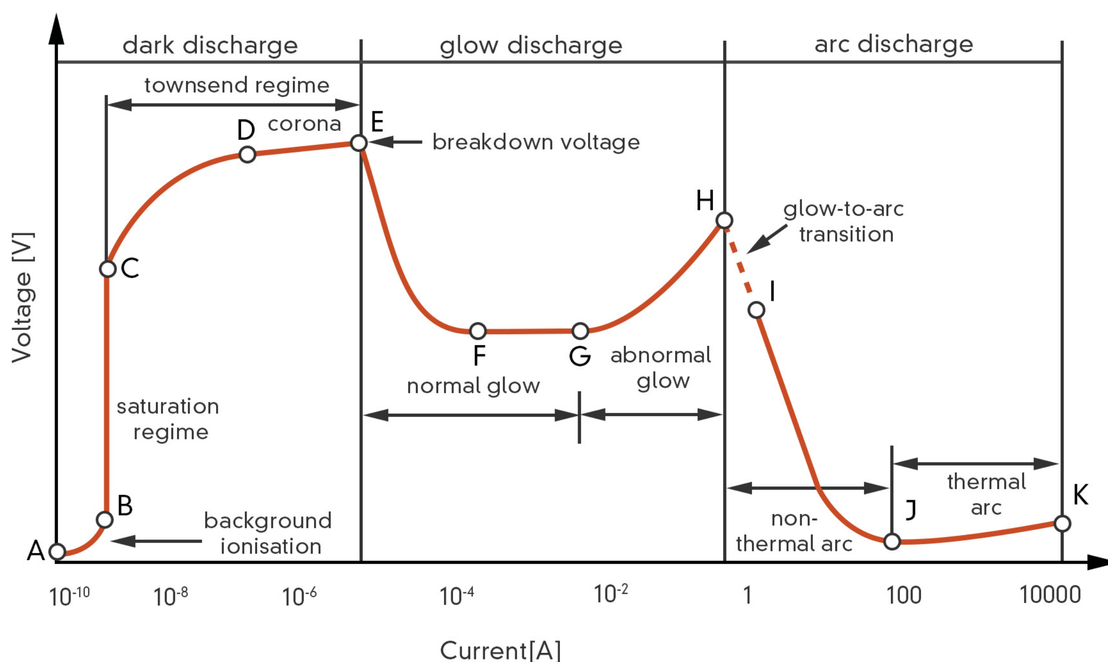

Figure 2.4: Schematic plasma voltage-currant characteristic [28], originally from [5].

and negative glow area, closed to the cathode, are relevant. The increasing discharge current also results in an increasing discharge voltage. This leads to the plasma discharge over the entire surface, predominantly near the edges and at cathode surface irregularities. The abnormal glow discharge area defines the operation range for sputtering, see point G in Fig. 2.4. By further increasing the current a transition point from glow to arc discharged is reached. The arc discharge zone is depending on the internal resistance of the power supply and is affected from thermionic emission of electrons at higher currents [5, 24, 29].

2.3 Sputtering

In sputter deposition the produced ions are attracted to the negatively charged target, eject solid source material atoms, and initiate an impact evaporation and partial ionization of the cathode material. These metal atoms and ions (ionization typically >1 % [30]) are transferred and accelerated towards the substrate, where they condense and form the film. Secondary electrons, which are also ejected from the target surface (due to ion bombardment from the target) contribute to further working gas ionization acting as primary electrons in the plasma [5, 27, 31].

An essential parameter describing the coating efficiency is the sputter yield, Y, which is defined as the ratio between the ejected atoms from the target and the incident ions on the substrate. The sputter yield is influenced by the energy of the incident ions, the masses of

ions and target atoms, the binding energy of atoms in solid state, and the angle of incidence of ions. Moreover, the chamber pressure, the substrate temperature, the target geometry, the distance between target and substrate, and the type of power supply substantially influence the glow discharge of conventional sputter systems [5, 24].

In order to form nitride or oxide coatings an additional gas component is necessary. Reactive processes are typically carried out in an Ar + N_2 or Ar + O_2 atmosphere. It is noteworthy that the coating properties are strongly dependent on the reactive gas partial pressure, and also strongly affected by chemical interactions of the introduced gas with the target material, which will be addressed later [5, 27]. At a lower chamber pressure, only few Ar ions hit the target, which yields in a decrease of the deposition rate. Therefore, the ionization efficiency is reduced. The other extreme is a higher chamber pressure which leads to a large number of collisions before they reach the substrate.

A certain problematic in reactive processes is the reaction of the cathode material with the introduced reactive gas. The time-dependent poisoning of the target has various effects on the process and film growth. When the reactive gas partial pressure is sufficiently high, a compound layer (e.g. TiN a Ti-cathode in a N_2 process) will form on the cathode surface. This layer usually exhibits a higher melting point than the solid cathode material. As a result, it prevents from droplet formation (molten macro-particles of the bulk material) on the arc spot and also reduces the number and size of sputtered atoms. The target state (i.e. metallic or poisoning) can be well identified by the voltage characteristic curve during the process. Typically, a hysteresis is observable when target poisoning occurs. At a certain nitrogen pressure (i.e. if, in time-average, there is a sufficiently high number of N ad-atoms on the surface), e.g. TiN is formed. The continuous coverage of the target surface results in a slowly increasing voltage, up to a saturation level. If the partial pressure of the reactive gas is now reduced, the voltage will not linearly decrease, as it takes time for the compound layer to be removed by particle bombardment. Summarizing, the adjusted gas flow rate, hence partial pressure of the reactive gas, can induce target poisoning. This, in further consequence, strongly affects the evaporation behavior [24, 32–34].

As has been mentioned before, the plasma consists of charged particles. Hence, it reacts upon the presence of magnetic fields. This fact is used to improve the deposition efficiency as well as growth kinetics. A magnetron, which is basically defined as a hot cathode (i.e. an electrode which is heated to emit electrons) centered in a vacuum tube, affects the electron movement, ideally resulting in an enhanced local ionization particle density caused by magnetic fields lines of the magnetron also results in a larger number of collisions of gas species. Benefits are a higher ion bombardment and an increasing sputter yield even with reduced gas pressure. Consequentially, each deposition system has its ideal chamber pressure and geometry at which deposition, under given process conditions, is most efficient. In general, one can

distinguish between two types of magnetrons: conventional balanced magnetrons (CBM) and unbalanced magnetrons (UBM). In a CBM all magnetic field lines reach from the outer to the inner magnetron section, meaning they are closed. On the contrary, in an UBM system not all field lines are closed, some may be directed towards the substrate, see Fig. 2.5.

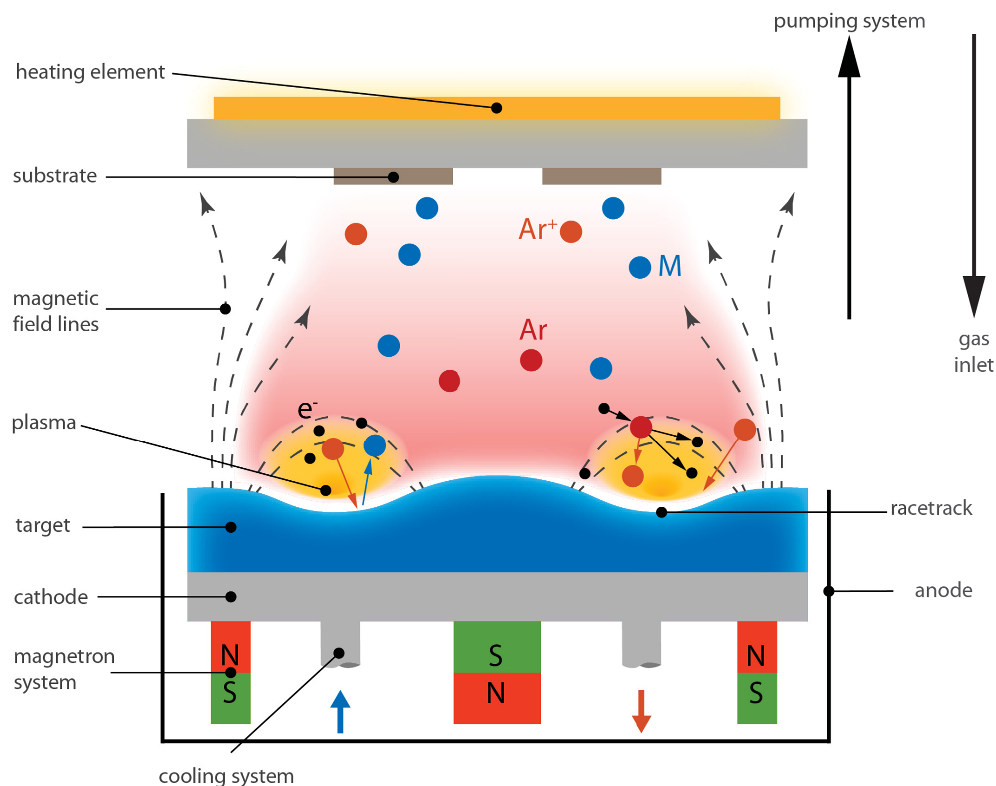

Figure 2.5: Unbalanced magnetron sputtering [28].

This arrangement allows the plasma to extend towards the substrate, also leading to Ar ion generation close to the substrate. A slightly negative substrate bias can then be used to attract these particles and affect growth kinetics, hence film properties. Additionally, the substrates may be heated to further improve diffusion. All those factors can be used to modify film growth, crystal structure, stress formation, film density, hence mechanical and thermal properties as explained in Chapter 2.4 [5, 27, 31].

2.3.1 DC sputtering

A direct current (DC) power supply is the easiest and rather cost-effective technology to deposit coatings. Thereby a constant direct current voltage of several hundred volts is applied between the negatively charged target (-) and the positively loaded chamber wall and substrate (+). However, due to possible charging of non-conductive components (e.g. target material) is limited to conductive materials. Thus, when using non conducting solid materials, the cathode and the substrates may build up a charged surface acting as a bar-

rier for arriving ions. As a consequence of the rejected particles the sputter process will be interfered and the sputter yield decreases, at worst it could lead to a process interruption. Another major issue of DC sputtering with non-conductive materials is the possibility of arcing. Arcing is identified as a low voltage and high current discharge. This can be counteracted with arc suppression units. Disadvantages in the formation of non-conducive layers with DC sputtering are elevated temperatures, which can damage the target by melting, and also the generation of droplets, which affect the thin film structure [5].

2.3.2 Pulsed DC sputtering

Pulsed DC sputtering is the most common sputter deposition technique. To prevent problems which occur in DC Sputtering, pulsed DC sputtering has been developed and is now a well-established alternative when processing non-reactive coatings, as well as a suitable alternative to a DC power supply in terms of arc preventing in reactive atmosphere. A typical voltage characteristic is presented in Fig. 2.6. Pulse frequencies are in the range of 10 to 350 kHz and duty cycles (i.e. sputtering period, which permit high power during the pulse and a cool down of the system between pulses) in the range of $50 - 90\%$.

The duration cycle (τ_{cycle}) starts with a small positive pulse (pulse time, τ_{rev}), which is used to reject ions from the surface in order to prevent a charge-build up. Subsequently, a high negative voltage is applied, representing the sputtering cycle, in order to initiate ion bombardment of the cathode. During this time it may be again recharged. Because of the relatively large difference in electron and ion velocities, the off-time, τ_{rev} be lower compared with on-time pulse, τ_{on}. A duration time rate of 1 to 10 is common. Furthermore, the cycle duration represents the lowest critical pulsing frequency ($f_c = 1/\tau_{cycle}$) [5, 27, 35].

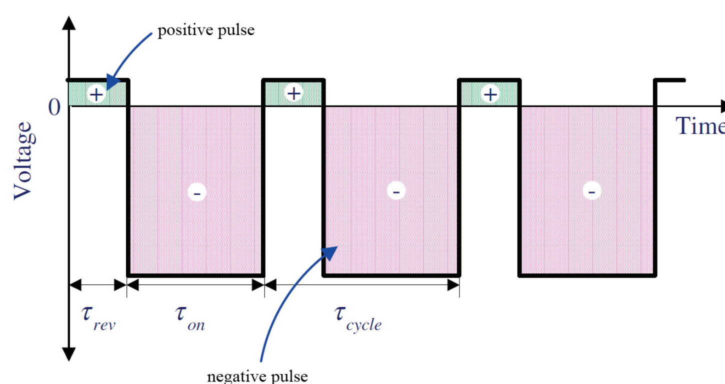

Figure 2.6: Schematic voltage characteristic of pulsed DC sputtering [35].

2.3.3 High power impulse magnetron sputtering

High power impulse magnetron sputtering allows for enhanced target material ionization in the range of 70 % [24, 30, 36–40] as compared with conventional pulsed DC of 1 % [24, 30, 36]. An extremely high power pulse is used to generate a large target power density of several $kWcm^{-2}$ in a relatively short period. In the case of conventional magnetron sputtering, the duration time rate is smaller than 10 %. Therefore, the cathode has to persevere a high peak power for a short time, followed by a long off-time in order to discharge and cool down. The peak current density of the target can reach a few Acm^{-2}, which is up to three times higher than for conventional DC sputtering. The discharge voltage reaches several hundred volts. The time-averaged target power density is in average similar to DC magnetron sputtering, which is important, in order to prevent the target and magnetron from damage [5, 24, 30, 41, 42].

There are two possibilities to avoid arcing during HiPIMS. First of all short pulses in the range of 5 to 20μs (in order remain in the glow discharge regime) are generated, followed by a long pre-ionization time with a low density plasma. In the time duration of high current the glow discharge persists in a transition mode, whereupon possible arcing events should be avoided. As a consequence, for instance, metal oxide films can be grown in a stable and arc-free deposition process. Alternatively a longer impulse (e.g. a few thousands of μs) can be applied. The last alternative route described here (Fig. 2.7), is divided into two areas, whereas the first one is weakly ionized for the formation of a stable discharge. The second highly ionized part should help to control the arcs [5, 42].

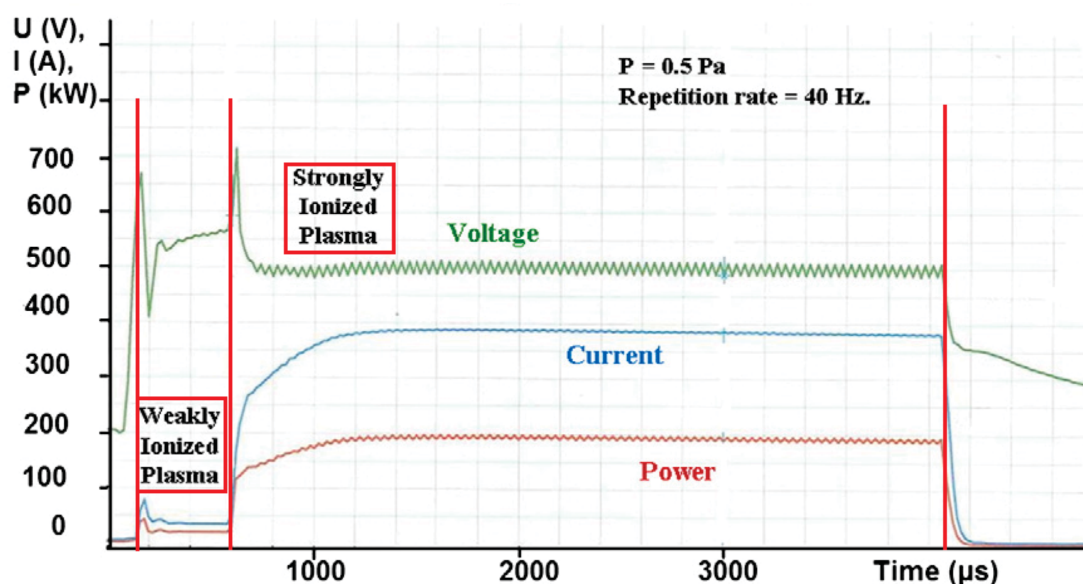

Figure 2.7: Target voltage and current waveforms during a long-pulse operation [42].

HiPIMS in combination or utilization with a bias potential is used to modify the structure

and film properties. In order of the high ion flux and with a low applied bias voltage it is applicable to achieve thick dense films with low stresses [24].

2.4 Thin film growth

2.4.1 Basics of nucleation and grain growth

Properties of thin films strongly depend on the deposition conditions and can be manipulated by controlling the substrate temperature, the chamber pressure, and energies of the sputtered species by means of the applied bias voltage. Film nucleation starts with the arrival of ions and vaporized atoms at the substrate surface. Ad-atoms diffuse along the surface until an energetically preferred location is reached, or they may re-evaporate after a certain time. In order to grow a film, the rate of arriving particles must exceed the rate of re-evaporated atoms. The more atoms arrive at the surface, the more likely they form larger clusters to reach a state in which the total surface energy is reduced. In the next step, the crystallite sizes increase with the continuous incorporation of impinging ad-atoms and atom clusters, consequentially also leading on increased island density. Subsequently, coalescence and secondary nucleation occur in which islands merge—preferred by high temperatures as diffusion is promoted. Coalescence, in turn, induces a reduction of the island density. Areas, which are (after coalescence) unoccupied may serve as new locations for further nucleation. Interfaces, which are initially incoherent, as for instance between islands, will persist during film growth, whereas small variations in crystallite orientations likely merge. With further deposition time (progressing film thickness), large islands grow together resulting in channels and holes at the interface. In the stadium of the secondary nucleation, channels and gaps are filled, forming a continuous dense thin film, on the basis of bulk diffusion [24, 27, 31].

The progress of film nucleation and growth is usually described by three concepts. These are distinguished by means of the binding energy between the film, substrate, and vapor, see Fig. 2.8.

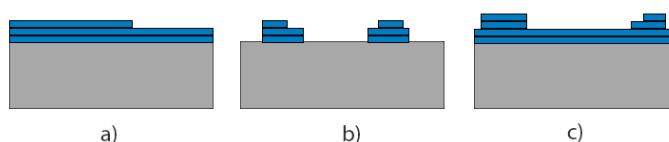

Figure 2.8: a) Layer-by-layer growth, b) 3D island growth, and c) mixed growth, adapted by [24].

The layer-by-layer growth or Frank-van der Merwe mode, Fig. 2.8a, is two dimensional. The formation of a new layer is initiated after covering the entire surface underneath, due to the

surface energy. This ideal film exhibits a very smooth surface, contrary to Vollmer-Weber, Fig. 2.8b, or 3D island growth. In this case, the binding energy of the deposited material is stronger than to the substrate. Ad-atoms on the surface will rapidly diffuse towards neighboring ad-atom cluster and remain there, forming islands. Stranski-Krastanov growth, Fig. 2.8c, is a combination of both and will most likely represent actual film growth. It takes place in two steps. The film growth starts with layer-by-layer and beyond a critical layer thickness a change to island growth occurs. [27, 31].

2.4.2 Structure zone model

Thin film structure and morphology can well be adjusted by various deposition parameters. A convenient way to connect all these parameters is the so-called structure zone model (SZM). The main features of the terminology of zone I, II and III originate from Movchan and Demchishin [5, 43]. Their SZM concept was developed for extremely high thickness ($>100\ \mu$m) of polycrystalline films. A reduced parameter—the homologous temperature, T_h—was later introduced, defined as the film growth temperature normalized by the melting temperature of the deposited material. Thornton [44] revised this model by considering the influence of the deposition pressure and substrate temperature on the microstructure. Also a transition zone, T, between zone I and II was introduced. A decade later Messier [45] declared the ion energy as additional factor. All previous reports indicate that the microstructure of zone III exists only for thin films in a non-pure ambit (i.e. existence of impurities) [46]. Because of rapidly increasing plasma-based deposition techniques such as high power impulse magnetron sputtering, the increased ion fluxed must also be taken into consideration. Mahieu first proposed such extended SZM [47]. The diagram has been updated by establishing the ad-atom mobility on one axis. However, the most up-to-date and nowadays widely-acknowledged SZM was published by Anders [48].

The structure zone model is a suitable tool to estimate film characteristics when changing certain deposition parameters. Generally, as described in the previous paragraph, it can be divided into 4 zones. At low energies representing Zone Ia, ad-atoms exhibit low mobility, which prevents them from overcoming the diffusion barrier. The incident particles arrive at the substrate surface at an angle α (see Fig. 2.9a). However, the growing atom clusters and columns cause shadowing effects, resulting in local porous and/or amorphous microstructure (angle β) without preferred growth orientation. By an improved bombardment a more dense columnar structure can be obtained. Zone Ib, Fig. 2.9b, is controlled by knock-on effects, which cause the voided structure to be filled up by particles. A structural change in Zone Ib is still not possible due to the insufficient thermal energy. Contrary, in Zone Ic, T, and II more mobile ad-atoms are induced by higher deposition temperatures. Hence, the sputtered species can diffuse on single grains in random out-of-plane orientation, but not from one grain to another. So grains will grow in a faceted columnar structure which only is

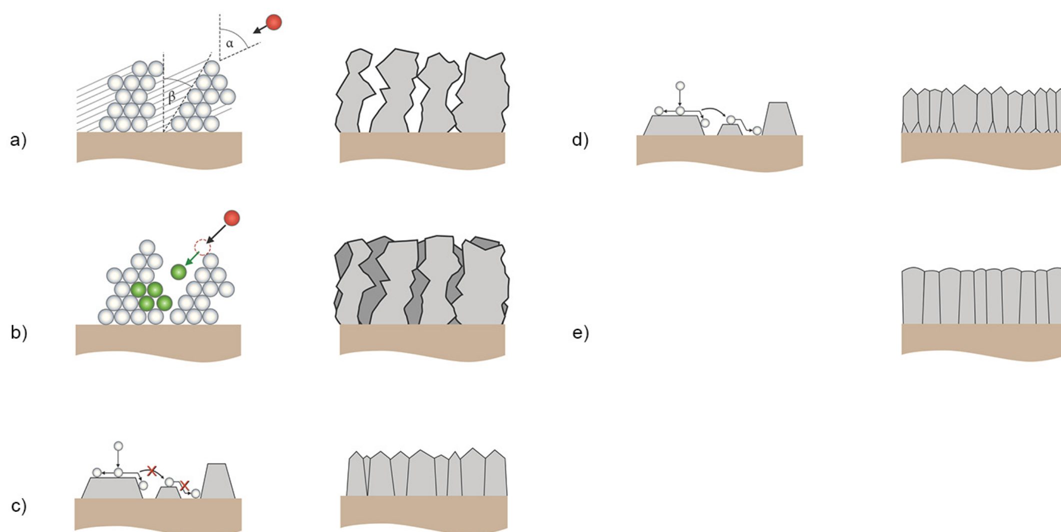

Figure 2.9: Schematic representation of various strucutre zones: a) zone Ia, b) zone Ib, c) zone Ic, d) zone T, e) zone II adapated from [49], originally from [47].

separated by grain boundaries, but, however, not by holes, Fig. 2.9c. In Zone T, Fig. 2.9d, the ad-atoms are allowed to diffuse beyond grain boundaries. The small polycrystalline grains in turn grow in faceted crystals and form uniform crystallographic planes. Finally, a complete thermodynamic stable thin film microstructure occurs in Zone II, Fig. 2.9e. Due to recrystallization more stable islands are formed and all columns are oriented with the plane of lowest surface energy [5, 24, 47].

This results in high particle collisions, caused by Ar ions and re-sputtered atoms. A continuously increasing kinetic energy implies a decreasing net deposition rate, until a certain stage is reached, at which material is re-ejected from the substrate. This effect may even be promoted by applying a negative substrate voltage and is typically used to clean the substrate and referred to as ion etching [5, 24, 28, 47, 48].

Anders modified and extended the axes of the SZM in a way that process related growth characteristics are taken into account, Fig. 2.10:

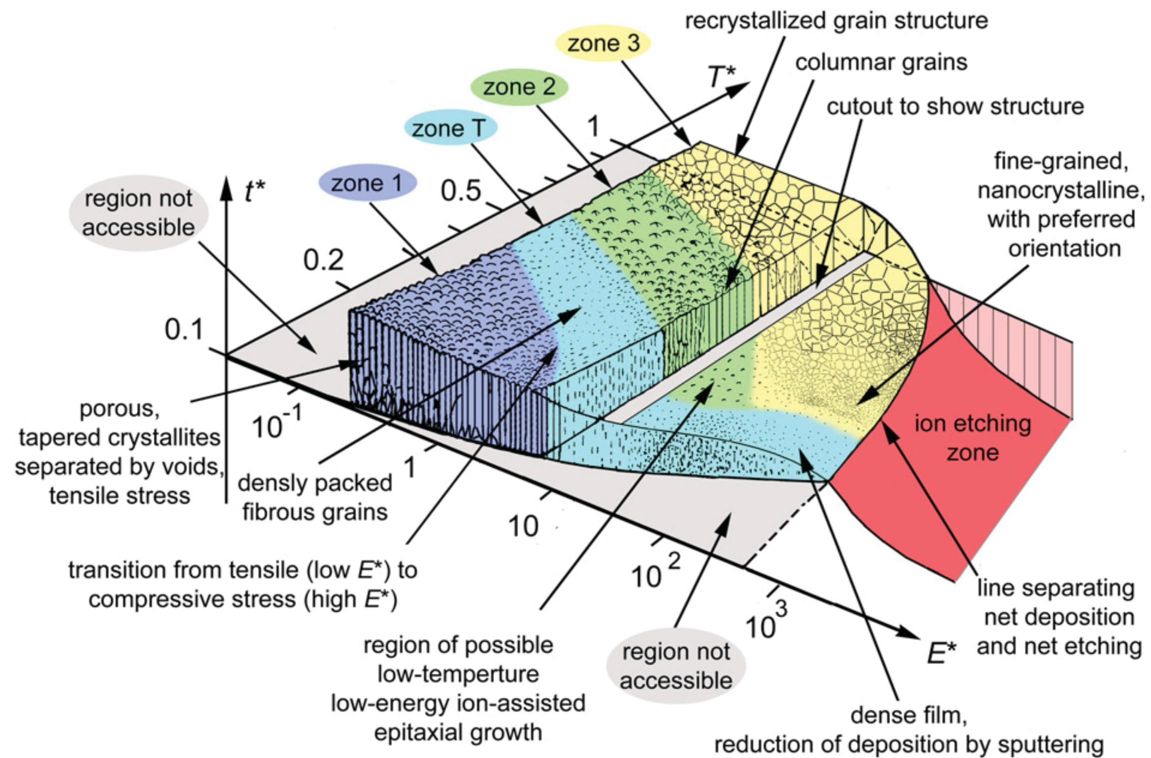

Figure 2.10: Extended structure zone model by Anders [48].

- the generalized temperature, T^*, consists of the homologous temperature and a temperature displacement induced by the potential energy of arriving particles
- the logarithmic-scaled normalized energy, E^*, replaces the linear pressure axis and includes the kinetic energy from displacement and heating effects caused, for instance by ion bombardment
- the net film thickness, t^*, on the z-axis, demonstrates an increase or decrease of the film thickness in succession of densification, sputtering, or ion etching.

Chapter 3

Coating systems

Hard ceramic-like coatings belong to an industrially important class of materials. Their chemical bonding character and resulting properties are summarized in Fig. 3.1. Depending on the position within the triangle of ionic, covalent, and metallic bonds, different material properties arise. Hence, those materials may also be denoted as metallic, ionic, or covalent hard materials. Prominent representatives for nowadays industrially applied hard ceramic-like coatings are transition metal nitrides (TMN) such as Ti-N and Cr-N. As they are located in between the covalent and metallic key points of the triangle, high hardness and strength can be expected. By alloying Aluminum ($Ti_{1-x}Al_xN$ and $Cr_{1-x}Al_xN$), a further improvement in terms of (thermal) stability can be achieved [21].

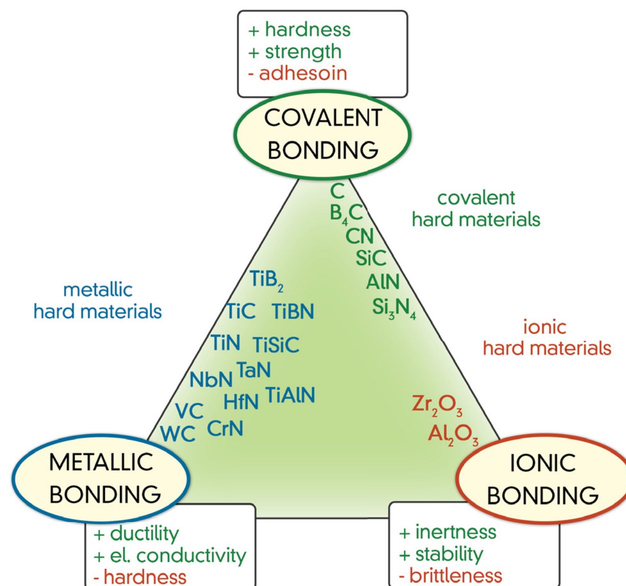

Figure 3.1: Hard ceramic-like coatings classified in terms of bonding character and mechanical properties adapted from [50], originally from [51].

Hard ceramic-like coatings are typically used in aerospace, tools and machining industry as well as in automotive application. TMN have been, and are still being studied intensively with respect to their physical, chemical, and mechanical properties. High thermal stability, good wear and corrosion resistance, as well as high hardness allow for a significant improvement of the bulk materials' properties, hence life time [21, 50, 52].

3.1 Ta

Tantalum (Ta) belongs to elements referred to as refractory metals and is nowadays used for various industrial applications particularly for electronic devices. Tantalum exhibits one of the highest melting points of all elements (3017 °C) [52]. In those applications where metallic Ta films are applied as diffusion barriers for copper in integrated circuits, in magnetic thin film applications, and wear protection, is required [1, 9, 14, 15]. Sputtered Ta thin films can occur in two different structures (Fig. 3.2): body centered cubic (bcc) α-Ta (space group: Im-3m, space group number: 229 [53]) and tetragonal structured β-Ta (P-421m, 113 [54]) [14, 19, 55–57]. The α-Ta modification has a low electric resistivity (15-80 $\mu\Omega$.cm), a hardness of $9-12$ GPa [55], and is resistant against high temperature wear and erosion. The β-Ta phase exhibits a higher electric resistivity up to $150-200\,\mu\Omega$.cm at lower temperatures, which therefore is often used as a distinction between these phases. However, β-Ta is unstable above temperatures of 750 °C and transforms irreversible into the bcc phase [55, 56, 58]. Even though β-Ta exhibits a higher hardness, 19.5 GPa, as compared with α-Ta, it is more brittle.

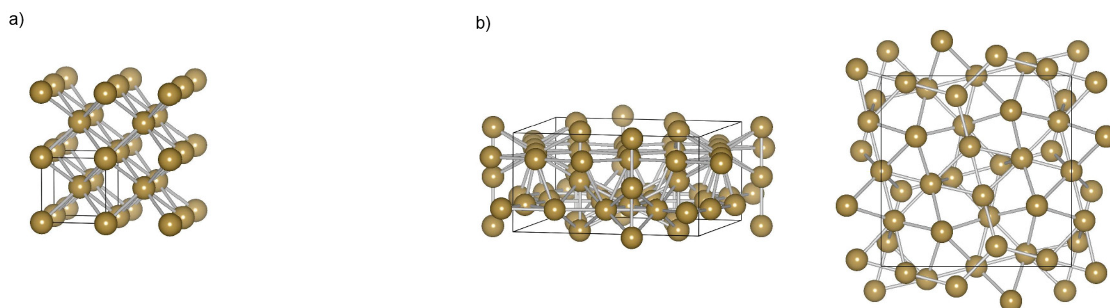

Figure 3.2: a) bcc Ta structure, b) tetragonal Ta structure [59].

3.2 TaN

TaN thin films deposited by PVD can be grown in various crystallographic modifications as can be assumed from the binary N-Ta phase diagram (Fig. 3.3). Beside the equilibrium phases α-Ta(N) (Im-3m, 229), hexagonal close packed (hcp) γ-Ta_2N (P-3m1, 164, ϵ-Fe_2N type), and hcp ϵ-TaN (P6/mmm, 191), several metastable phases exist: bcc β-Ta(N)

(P42/mnm, 136), hexagonal (hex) Ta_2N (P63/mmc, 194), hex θ-TaN (WC-type), cubic B1 δ-TaN ($Fm\overline{3}m$, 225, NaCl type), hex Ta_5N_6 (P63/mcm, 193, Nb_5N_6 type), tetragonal Ta_4N_5 (I4/m, 87), and orthorhombic Ta_3N_5(Cmcm, 63), which all have similar characteristics [9, 19, 21, 52].

Noteworthy is the thermodynamically stable stoichiometric TaN phase. Additionally, several under- or overstoichiometric Ta-N phases can occur, which strongly depends on the deposition conditions and process parameters.

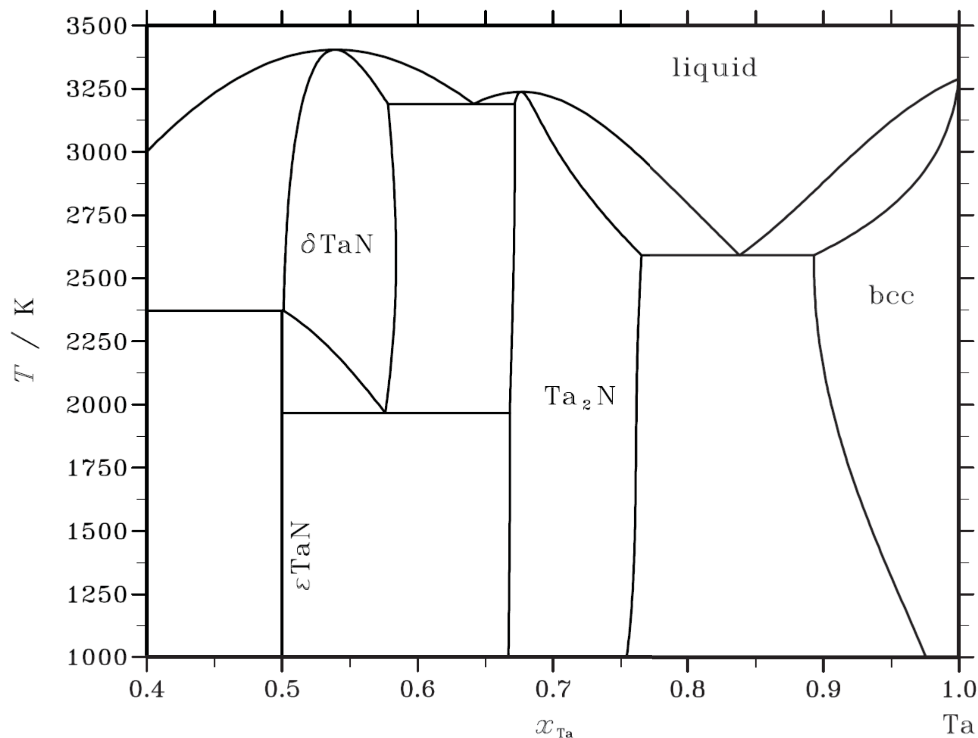

Figure 3.3: TaN [60].

Howsoever, the most utilized application, as diffusion barrier layer in copper metallization of silicon integrated circuits, raised in effectiveness, as the nitrogen content increases, until a N to Ta ratio of 1:1 appears also at elevated temperatures [21, 52]. More recently, Ta-N finds applications in manufacturing of chemical apparatus, and medical implants [10]. Other common application areas, related to their to their excellent mechanical properties, are cutting tools or helicopter gearboxes and compressor blades [12, 14–16].

Chapter 4

Characterization techniques

4.1 Coating thickness measurement

The coating thickness is an essential factor of technological thin films for protective applications. Two methods to gain information on the coating thickness were used in this work: ball-crater-test (Fig. 4.1) and direct measurements from cross-section images obtained by scanning electron microscopy.

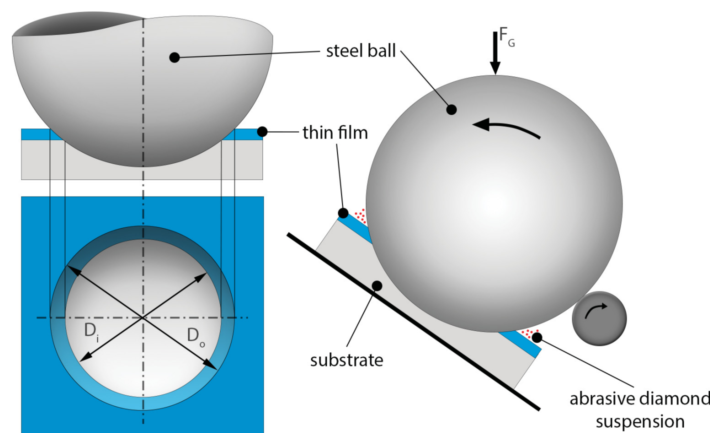

Figure 4.1: Schematic of a ball-crater-test.

The ball-crater-test is a simple and straightforward method. A polished steel ball (in this case with a diameter $D = 30\,\text{mm}$) is pressed onto the coating sample with its net weight. An abrasive diamond suspension is enclosed to the point of contact. Then the ball is set into rotation. Thereupon material is removed until the substrate material is exposed. The resulting crater exhibits an inner (D_i) and outer (D_o) diameter, which are determined by

optical light microscopy. The coating thickness can be calculated according to equation 4.1.

$$h = \frac{(D_o^2 - D_i^2)}{4D} \tag{4.1}$$

4.2 X-ray diffraction

X-ray diffraction (XRD) is the most widely used non-destructive method to determine the structure of a solid material or thin film. Basically, two specific X-ray-types arise from the interaction of electrons with the inner shells of an atom (i.e. the anode material of the X-ray source), thermally generated at the cathode, with a solid anode material. One is the continuous radiation, covering a broad wavelength spectrum. The second one is the characteristic, element-specific, radiation. It arises from kick out processes of electrons from an inner shell. The generated vacant electron position is re-occupied by an electron from an outer shell. This transition results in the emission of characteristic electromagnetic radiation, which is then directed towards the sample. X-rays arrive there at a certain angle and interact with electrons of the solid material. Depending on given local atomic conditions, the electromagnetic waves can either constructively or destructively interfere. At a given wavelength λ, the lattice plane distance d_{hkl}, at which constructive interference occurs, is clearly defined according to Bragg's law 4.2.

$$n\lambda = 2d_{hkl}\sin\theta \tag{4.2}$$

n is the diffraction order, λ the electromagnetic wavelength of the anode material —in this specific case Cu ($\lambda(K_\alpha) = 0.15406\,\mathrm{nm}$)—$d_{hkl}$...lattice plane distance [nm] and Θ...the Bragg angle [deg].

Naturally, a variation in the wavelength also results in a variation of angles or lattice plane distances which fulfill the Bragg's law, illustrated in Fig. 4.2c. Therefore, the use of monochromatic X-rays is essential for a good spatial peak resolution. In addition to the monochromator, which may be placed after the X-ray source and optionally just before the detector, a mirror device (Göbel-Mirror), to ensure parallel beams, is placed in between the monochromator and the sample.

Two different measurement arrangements were used in this work to gain information on the crystallographic constitution of coatings deposited. The Bragg-Brentano arrangement is defined by a synchronously movement of the X-ray tube and the detector, whereby the scattering vector, g, is fixed exactly in the middle. Lattice planes parallel to the sample surface and normal to g fulfill the Bragg condition of. The source is performing a circular movement confining an angle θ with the sample surface plane. The angle 2θ, as shown in Figure 4.2a, between X-ray source and detector is fixed. For grazing incidence diffraction

(GID), Fig. 4.2b, the X-ray tube is stationary (constant angle of incidence) whereas the detector moves with 2θ. In that case, the scattering vector moves with θ. In this arrangement, lattice planes which are not parallel to the sample surface contribute to the XRD pattern. This arrangement identifies near-surface information about the sample. Contrary to Bragg-Brentano, including primarily depth information, which, however, leads to the disadvantage of intense substrate information in thin films measurements [61, 62].

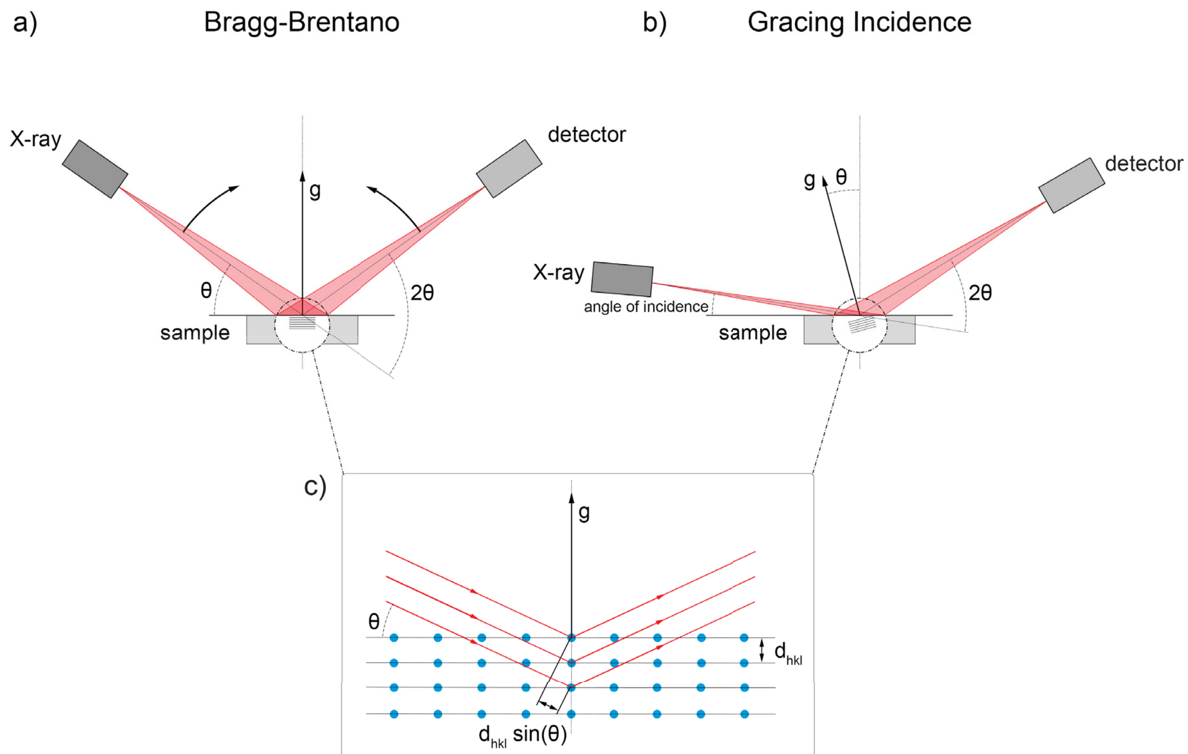

Figure 4.2: a) Bragg-Brentano arrangement, b) grazing incidence arrangement, c) schematic arrangement of Bragg's diffraction adapted from [49], originally from [61].

The obtained X-ray spectra can be used to obtain a multitude of information from the coating as illustrated in Fig. 4.3.

The distance of a certain lattice plane family {h,k,l}, d_{hkl}, is calculated by the diffraction angle 2θ of the respective XRD peak position (Fig. 4.3a) according to the Bragg formula. However, the exact peak position may varies from the ideal position due to the residual stress state, chemical variations, or defects within the coating.

As for the stress state, is has to be noted, that only strains are measured out of which stresses can be estimated. In case of compressive stresses and a Bragg-Brentano arrangement, the actual XRD peak is shifted to smaller diffraction angles as the lattice planes, for which the Bragg equation holds true, diverge (assuming only lattice planes parallel to the surface to obey Bragg equation). Conversely, tensile stresses cause a peak shift to higher diffraction

angles due to the decrease in lattice plane distances.

Similarly statements of chemical conditions can be made. For instance, peaks for a single-phased cubic $Ti_{0.5}Al_{0.5}N$ (Fig. 4.3b) film will lie in between the International Center for Diffraction Data (ICDD) peak positions for cubic TaN (larger lattice parameter, hence smaller diffraction angles) and cubic AlN (smaller lattice parameter, hence higher diffraction angles). However, heavy elements may be overestimated due to their large number of electrons which considerably interfere with the incident X-rays.

Moreover, the peak height gives a semi-quantitative explanation of the detected lattice planes. For example, the peak with the highest intensity can indicate the preferred orientation of the sample (Fig. 4.3c).

A commonly used parameter to estimate for the morphology of a thin film is the peak width (Fig. 4.3d). A single crystal or a big grain reflects in XRD patterns in a narrow peak and is defined by a low value of full width of half maximum (FWHM). Contrarily, a polycrystalline material exhibits a large number of small, randomly oriented crystals which result in broad peaks [61, 62].

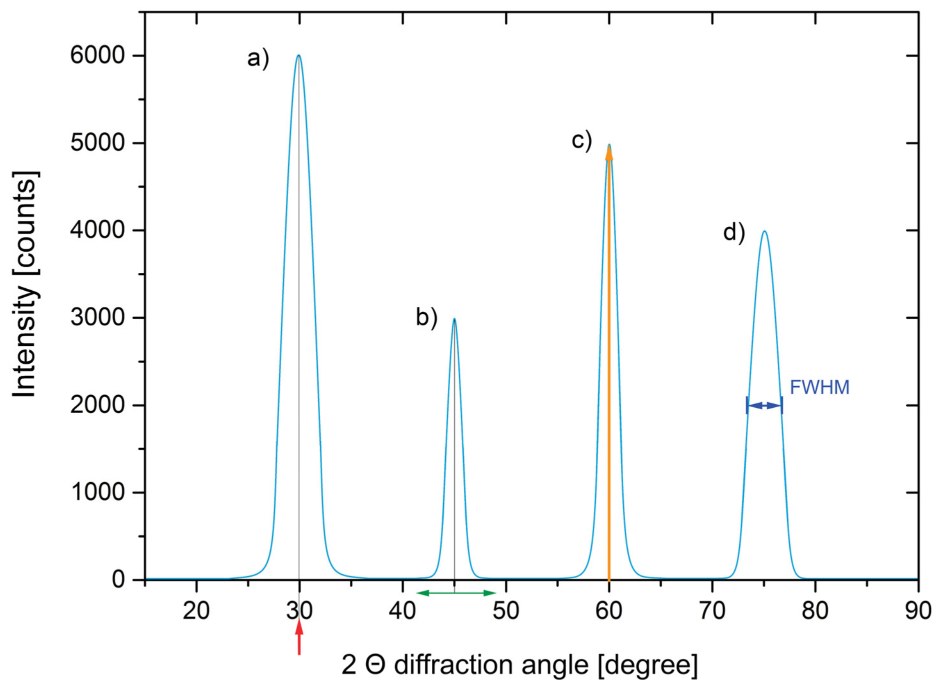

Figure 4.3: Schematic XRD pattern a) peak position, b) peak shift, c) peak height, and d) peak width (FWHM), according to [62].

4.3 Nanoindentation

In this study we used an IBIS nanoindentation system by Fischer-Cripps Laboratories for hardness and indentation modulus evaluation. The device is equipped with a Berkovich diamond tip, a three sided, geometrically self-similar pyramid, with a tip angle of 65.3 deg.

During the measurement the tip is pushed onto the film surface and a load-displacement curve is recorded (Fig. 4.4). Loads from 30 to 2 mN, depending on the film thickness were used. It is of utmost importance to exclude substrate interference. Therefore, it is necessary to bear the indentation depth in mind, typically 10% is considered as the maximum value [63]. At the maximum elastic-plastic load the indenter penetrates with the maximum indentation depth, h_{max}, consisting of elastic indentation depth, h_e, and plastic indentation depth, h_r. During the following load discharge only the plastic indentation depth can be determined from the residual contact area (likewise Vickers hardness). Subsequently, hardness and indentation modulus can be calculated (e.g. by the method of Oliver and Pharr [64]).

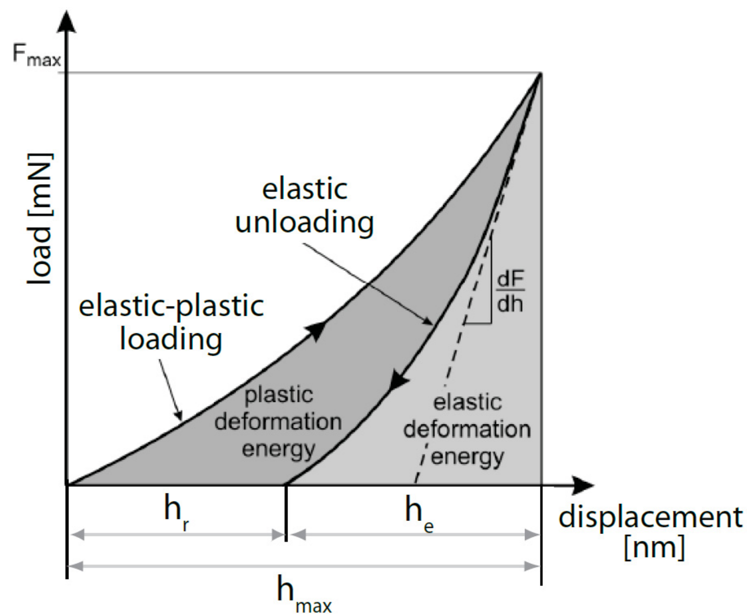

Figure 4.4: Schematic diagram of a load-displacement curve [65].

However, a multitude of factors may negatively influence the evaluation of nanoindentation measurements. In reality one will always have to deal with—to a certain extent blunt tip—. Thus, the actual deviation from the ideal tip has to be corrected taking the so-called area function (calibration with a reference material) into account. Furthermore, nanoindentation is very sensitive for surface irregularities such as droplets, growth defects, or steps within the film surface. To obtain reliable information on the coatings properties it is therefore of utmost importance to select clean and representative surface areas or, if not available, polishing of the sample surface is required. In addition, one may select the indentation

points by hand using a mapped-indentation grid. The influence of thermal drift hast to be minimized by an acclimatization time prior to each measurement. Moreover, vibrations can also cause fluctuations. The stress state of the coating also influences to higher hardness values and is often specifically adapted by selecting appropriate deposition conditions [63]. In the case of Ta-N, we observe high residual stresses, which can be influenced by grain boundaries or cracks in the material [63, 66, 67].

4.4 Scanning electron microscopy

Scanning electron microscopy (SEM) thin film investigations in this work are focused on surface and cross-sectional imaging. The latter one can be used for thickness evaluation as well as detailed insights into the coatings micostructure. In contrast to white-light microscopy, SEM allows for higher spatial resolution.

An electron source (field emission cathode with Schottky Emitter (LaB_6)) emits a beam of electrons, which are then accelerated by an electric field, (typically between 5 and 20 kV), depending on the specific purpose, and are subsequently focused on the sample by a system of magnetic lenses. This arrangement enables a defined beam movement (scanning of the sample surface). The sample itself is placed in an evacuated chamber to minimize interactions with air molecules. Different electrons matter interacts are known (Fig. 4.5).

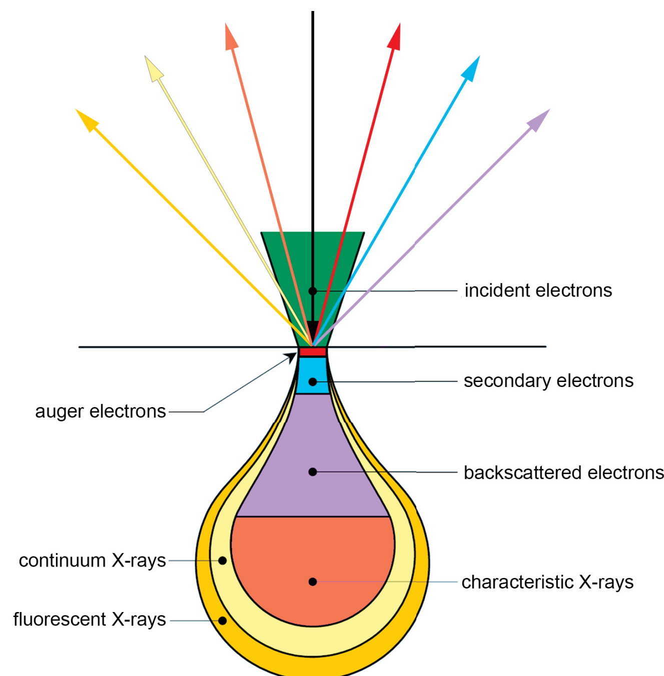

Figure 4.5: Interaction of the electron beam with the sample and corresponding information of generation depth out of the specimen used for materials characterization [68].

Close to the surface, emitted electrons, including secondary electrons (e.g. electrons emitted from external excitation of inner shell) and Auger electrons (electrons emitted from excess energy of a charge transfer of an outer to an inner shell), occur. They are in-elastically scattered. Back-scattered electrons emerge from an increased sample depth. These electrons are reflected from sample material by elastic scattering and are typically used for material contrast images for heavy elements. X-rays (i.e. characteristic X-rays, continuum X-rays, Fluorescent X-rays) arise from the highest sample depth. The characteristic X-rays are used for chemical analyses, as for instance energy-dispersive X-ray spectroscopy (EDS) or wavelength dispersive X-ray spectroscopy (WDS).

An even better resolution can be obtained by thermal field electron emission with the benefit of a higher and more stable beam intensity. Additionally, the spread in electron energy may be significantly reduced. Undesired charging of the sample is an issue, especially for non-conductive samples. For this reason, the respective sample may be sputtered with a conductive layer (e.g. Pt, Au) prior to the investigation. The detected electrons and X-rays are computationally processed. A major advantage hereby is the possibility to obtain information on the chemical composition in a rather simple, and non-destructive way. Electrons with sufficient kinetic energy strike an electron from an inner shell of the atom (see Fig. 4.6). The thereof remaining vacant energy level is subsequently occupied by an electron from an outer shell, which in term results in the emission of characteristic X-rays according to the energy difference. These characteristic X-rays exhibit a certain, element specific, energy related to a defined atomic transition. The number of counts is plotted against the respective energy, and used for element identification [69, 70].

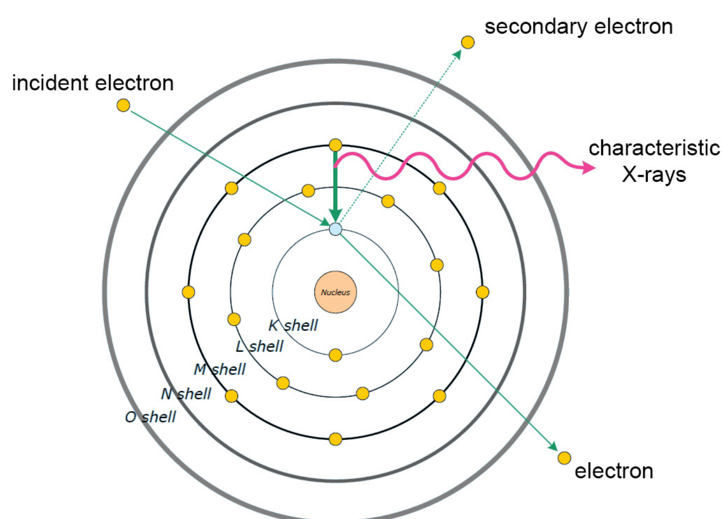

Figure 4.6: Generation of characteristic X-rays and secundary electrons based on the impact of accelerated electrons, adapted from [68].

Bibliography

[1] K. Radhakrishnan, N. Geok Ing, and R. Gopalakrishnan, Mater. Sci. Eng. B **57**, 224 (1999).

[2] R. E. Hampy, Transactions on Parts, Hybrids, and Packaging (1975).

[3] K. Eda, T. Miwa, Y. T. A, and I. Tomokl, IEEE Transactions of Microwave Theory and Techniques (1990).

[4] G. A. Patrizi, Thin Solid Films **291**, 513 (1996).

[5] P. M. Martin, *Handbook of deposition technologies for films and coatings: science, applications and technology*, 3rd ed., Vol. 3 (Elsevier Inc., 2009) p. 922.

[6] H. Holleck, "Advanced concepts of PVD hard coatings," (1990).

[7] A. Anders, Surf. Coatings Technol. **205**, S1 (2011).

[8] S. Tsukimoto, M. Moriyama, and M. Murakami, Thin Solid Films **460**, 222 (2004).

[9] X. Liu, G. Ma, G. Sun, Y. Duan, and S. Liu, Appl. Surf. Sci. **258**, 1033 (2011).

[10] L. Gladczuk, A. Patel, J. D. Demaree, and M. Sosnowski, Thin Solid Films **476**, 295 (2005).

[11] K. Holloway and P. M. Fryer, Appl. Phys. Lett. **57**, 1736 (1990).

[12] S. Kim and B. Cha, Thin Solid Films **475**, 202 (2005).

[13] Y.-I. Chen, B.-L. Lin, Y.-C. Kuo, J.-C. Huang, L.-C. Chang, and Y.-T. Lin, Appl. Surf. Sci. **257**, 6741 (2011).

[14] C. Stampfl and A. Freeman, Phys. Rev. B **71**, 024111 (2005).

[15] K.-Y. Liu, J.-W. Lee, and F.-B. Wu, Surf. Coatings Technol. **382232** (2014).

[16] G. Ma, G. Lin, S. Gong, X. Liu, G. Sun, and H. Wu, Vacuum **89**, 244 (2013).

[17] J. An and Q. Zhang, Surf. Coatings Technol. **200**, 2451 (2005).

[18] G. Lee, H. Kim, H. Choi, and J. Lee, Surf. Coatings Technol. **201**, 5207 (2007).

[19] N. Terao, Jpn. J. Appl. Phys. **10**, 248 (1971).

[20] C. Shin, Y. Kim, D. Gall, J. E. Greene, and I. Petrov, Thin Solid Films **402**, 172 (2002).

[21] P. H. Mayrhofer, C. Mitterer, and H. Clemens, Adv. Eng. Mater. **7**, 1071 (2005).

[22] E. Lugscheider, O. Knotek, C. Barimani, and H. Zimmermann, Surf. Coatings Technol. **94-95**, 641 (1997).

[23] S. Baragetti, Int. J. Fatigue **29**, 1893 (2007).

[24] P. H. Mayrhofer, *Skriptum zur Vorlesung: Oberflaechentechnik* (TU Wien, 2014).

[25] University of Warwick, *Plasma state of matter, http://www2.warwick.ac.uk/fac/sci/physics/current/teach/module_home/px384/chapter4*.

[26] A. Anders and A. P. Ehiasarian, *Talk at ICMCTF 2014, Ionized PVD: From Arcs to HIPIMS* (San Diego, 2014).

[27] W. Westwood, *Sputter Deposition* (AVS, 2003).

[28] C. M. Koller, *Thermal stability and oxidation resistance of Ti-Al-N / Ta-Al-N multilayer coatings*, Diploma thesis, Montanuniversität Leoben (2012).

[29] O. Mutaf-Yardimci, A. V. Saveliev, A. a. Fridman, and L. a. Kennedy, J. Appl. Phys. **87**, 1632 (2000).

[30] A. Anders, Surf. Coatings Technol. **204**, 2864 (2010).

[31] M. Ohring, *The Materials Science of Thin Films* (1992) p. 742.

[32] S. Harris, E. Doyle, Y.-C. Wong, P. Munroe, J. Cairney, and J. Long, Surf. Coatings Technol. **183**, 283 (2004).

[33] M. Kumar, S. Mishra, and R. Mitra, Surf. Coatings Technol. **228**, 100 (2013).

[34] L. Combadiere and J. Machet, Surf. Coatings Technol. **52**, 145 (1996).

[35] A. Belkind, A. Freilich, J. Lopez, Z. Zhao, W. Zhu, and K. Becker, New J. Phys. **7**, 90 (2005).

[36] J. Alami, K. Sarakinos, F. Uslu, and M. Wuttig, J. Phys. D. Appl. Phys. **42**, 015304 (2009).

[37] J. M. Schneider, U. Helmersson, V. Kouznetsov, K. Maca, and I. Petrov, Surf. Coatings Technolog. **122**, 290 (1999).

[38] A. Ehiasarian, R. New, W.-D. Münz, L. Hultman, U. Helmersson, and V. Kouznetsov, Vacuum **65**, 147 (2002).

[39] S. Konstantinidis, J. P. Dauchot, M. Ganciu, a. Ricard, and M. Hecq, J. Appl. Phys. **99**, 013307 (2006).

[40] V. Sittinger, F. Ruske, W. Werner, C. Jacobs, B. Szyszka, and D. Christie, Thin Solid Films **516**, 5847 (2008).

[41] J. Alami, P. Eklund, J. Andersson, M. Lattemann, E. Wallin, J. Bohlmark, P. Persson, and U. Helmersson, Thin Solid Films **515**, 3434 (2007).

[42] K. Sarakinos, J. Alami, and S. Konstantinidis, Surf. Coatings Technol. **204**, 1661 (2010).

[43] B. Movchan and A. Demchishin, *Phys. Met. Metallogr. 28* (1969) p. 653.

[44] J. A. Thornton, J. Vac. Sci. Technol. **11**, 666 (1974).

[45] R. Messier, J. Vac. Sci. Technol. A Vacuum, Surfaces, Film. **2**, 500 (1984).

[46] P. Barna, *Diagnostics and Application of thin films*, edited by I. R. L. Eckertova (1992) pp. 295–309.

[47] S. Mahieu, P. Ghekiere, D. Depla, and R. De Gryse, Thin Solid Films **515**, 1229 (2006).

[48] A. Anders, Thin Solid Films **518**, 4087 (2010).

[49] C. M. Koller, *The role of engetics and kinetics for phase evolution of aluminium oxide based materials*, Phd thesis, Vienna University of Technology (2015).

[50] M. Schlögl, *Multilayer Design for Increased Toughness of CrN-based Coatings*, Phd, Montanuniversität Leoben (2012).

[51] H. Holleck, Surf. Eng. Sci. Technol. I , 207 (1999).

[52] A. E. Kaloyeros and E. Eisenbraun, Annu. Rev. Mater. Sci. (2000).

[53] K. Lejaeghere, V. Van Speybroeck, G. Van Oost, and S. Cottenier, Crit. Rev. Solid State Mater. Sci. **39**, 1 (2014).

[54] A. Arakcheeva, G. Chapuis, and V. Grinevitch, Acta Crystallogr. Sect. B Struct. Sci. **58**, 1 (2001).

[55] J. Lin, J. J. Moore, W. D. Sproul, S. L. Lee, and J. Wang, IEEE Trans. Plasma Sci. **38**, 3071 (2010).

[56] Y. Danon, C. Lee, C. Mulligan, and G. Vigilante, IEEE Trans. Magn. **40**, 1826 (2004).

[57] L. Gladczuk, A. Patel, C. Singh Paur, and M. Sosnowski, Thin Solid Films **467**, 150 (2004).

[58] D. W. Matson, E. D. Mcclanahan, J. P. Rice, S. L. Lee, and D. Windover, Surf. Coatings Technolog. , 411 (2000).

[59] *Private communications with David Holec, Vienna University of Technology, 23.11.2014*.

[60] Scientific Group Thermodata Europe (SGTE), *Thermodynamic Properties of Inorganic Materials compiled by SGTE*, volume 19 ed., edited by L. fur Werkstoffchemie and R.-W. T. H. Aachen (2006).

[61] Y. Waseda, E. Matsubara, and K. Shinoda, *Zhurnal Eksp. i Teor. Fiz.* (2011) p. 322.

[62] J. Keckes, *Skriptum zur Vorlesung: Microstructure and diffraction method* (MUL, 2009).

[63] A. Fischer-Cripps, A. E. Bergles, G. A. Klutke, K. K. Wang, I. Finnie, and H. T. Yang, *Profiles Drug Subst. Excip. Relat. Methodol.*, Vol. 36 (2011) p. 302.

[64] W. C. Oliver and G. M. Pharr, Journal of Materials Research , 1564 (1992).

[65] H. Riedl, *Phase Stability and Mechanical Properties of Yttrium alloyed Ti-Al-N Thin Films*, Diploma thesis, Montanuniversität Leoben (2012).

[66] A. Fischer-Cripps, Surf. Coatings Technol. **200**, 4153 (2006).

[67] W. D. Nix, Materials Science and Engineering **236** (1997).

[68] JEOL, *Energy Table for EDS Analysis, http://www.jeol.com* (2013).

[69] J. J. Friel, *X-ray and image analysis in electron microscopy* (2003) p. 97.

[70] R. Egerton, *Physical Principles of Electron Microscopy* (2005) p. 207.

Publication I

Structure, phase evolution and mechanical properties of HiPIMS, pulsed DC and DC sputtered Ta-N films

H. Marihart, C.M. Koller, R. Rachbauer, P. Polcik, P.H. Mayrhofer

Manuscript in final preparation.

Structure, phase evolution and mechanical properties of HiPIMS, pulsed DC and DC sputtered Ta-N films

H. Marihart,[1,*] C.M. Koller,[1] R. Rachbauer,[2] P. Polcik,[3] and P. H. Mayrhofer[1,4]

[1] *Christian Doppler Laboratory for Application Oriented Coating Development at the Institute of Materials Science and Technology, Vienna University of Technology, A-1060 Vienna, Austria*

[2] *Oerlikon Surface Solutions AG, LI-9496 Balzers, Liechtenstein*

[3] *Plansee Composite Materials GmbH, D-86983 Lechbruck am See, Germany*

[4] *Institute of Materials Science and Technology, Vienna University of Technology, A-1060 Vienna, Austria*

(Dated: March 5, 2015)

The microstructural development of reactively sputtered tantalum nitride thin films is investigated as a function of the N_2-to-total pressure ratio (p_{N2}/p_T) and the operating mode of the metallic tantalum cathode by high power impulse magnetron sputtering (HiPIMS), pulsed direct current (DC) and DC sputtering. For all sputtering modes investigated, the phase evolution of the Ta-N films strongly depends on the nitrogen partial pressure, p_{N2}, used when keeping the total pressure, p_T, constant at 0.3 or 0.6 Pa. The major crystalline phases identified, with increasing the N_2-to-total pressure ratio, are α- and β-Ta, orthorhombic o-Ta_4N, hexagonal close packed (hcp) γ-Ta_2N, cubic δ-TaN, and hcp ϵ-TaN, respectively. The minimum p_{N2}/p_T-ratio needed for the formation of the individual nitride phases, decreases from DC to HiPIMS. For example, when using a p_{N2}/p_T-ratio of 13.4%, the nitrogen content within the HiPIMS film is $\approx$ 38.5 at.%, but only $\approx$ 26.5 at.% within the pulsed DC and DC sputtered films. Therefore, the HiPIMS film is mainly composed of γ-Ta_2N (with traces of ϵ-TaN) whereas the pulsed DC and DC sputtered films also contain o-Ta_4N next to γ-Ta_2N. These coatings—with a majority of γ-Ta_2N—exhibit the highest hardness values with 38.2 ± 4.6, 38.0 ± 2.3, and 40.0 ± 3.8 GPa among all samples studied, respectively. Further increasing p_{N2}/p_T leads to the formation of δ- and ϵ-TaN, which are the dominating phases for p_{N2}/p_T-values above 38.1%. For higher N_2-to-total pressure ratios, the phase fraction of ϵ-TaN increases on the expanse of δ-TaN and a significant reduction in hardness, even down to $\approx$ 20 GPa, is observed. Based on our results we can conclude that the highest hardness is obtained forγ-Ta_2N dominated films. Consequently, with respect to mechanical properties, the most important p_{N2}/p_T range is between 13.4 and 38.1%, where the films undergo a transformation from γ-Ta_2N (plus o-Ta_4N) to δ- and ϵ-TaN. Generally, this phase transformation is shifted to lower p_{N2}/p_T-values when using HiPIMS instead of pulsed DC or DC sputtering.

Keywords: TaN; Phase Evolution; HiPIMS; γ-Ta_2N;

I. INTRODUCTION

Transition metal nitrides processed by physical vapor deposition (PVD) exhibit remarkable properties making them attractive candidates for a vast number of industrial applications [1–7]. Most prominent representatives are TiN [8–10], CrN [10–12], and their Al-alloyed ternary systems $Ti_{1-x}Al_xN$ [10, 13–18] and $Cr_{1-x}Al_xN$ [10, 11], which are nowadays used for cutting and drilling operations. Also tantalum forms binary and ternary (Al) nitrides which are extensively studied concerning electric and thermal properties in recent years. Accordingly, research of Ta-N is mainly driven by the microelectronic sector because of its applicability in thin film resistors and diffusion barriers in Cu-based metallization [19–26]. Recent studies also emphasize on its wear and corrosion resistance, excellent hardness, and high thermal stability [7, 21, 23–25, 27, 28]. Furthermore, Ta-N films exhibit a huge potential for chemical apparatus, medical implants [19, 29], mechanical demanding applications including compressor blades, helicopter gearboxes, or in the tool coating industry as for instance high-speed cutting and drilling [21, 23, 25, 26, 28, 30].

Material properties, and in further consequence the accessible fields of application strongly correlate with the microstructure and crystallographic constitution. Among the most important phases, in the tantalum nitride binary phase diagram, are the solid solution α-Ta(N), hexagonal-close-packed (hcp) γ-Ta_2N (ϵ-Fe_2N-prototype), and hcp ϵ-TaN. Apart from these, a large number of metastable phases exist: body-centered cubic (bcc) β-Ta(N), hcp Ta_2N, hexagonal (hex) θ-TaN (WC-prototype), cubic B1 δ-TaN (NaCl-prototype), hex Ta_5N_6 (Nb_5N_6-type), tetragonal Ta_4N_5, and orthorhombic Ta_3N_5 [21, 23, 25, 26, 31–34]. For example, α-Ta is used as low resistant diffusion barrier, for high temperature wear and erosion application, or a protective gun-barrel coating [35]. The β-Ta phase is applied as thin-film resistor component because of the rather small temperature dependence of electrical properties over a wide temperature range [35]. It furthermore features reasonable good magnetic properties [36, 37]. One of the major fields of application of tantalum nitride phases are

* heribert.marihart@stud.unileoben.ac.at

electronic devices. Cubic δ-TaN, for instance, attracts attention due to its superconductivity [38], Ta_3N_5 finds use in the semiconductor industry, and the two phases hexagonal Ta_5N_6 and hcp ϵ-TaN exhibit a strong hybridization between N and Ta atoms, which makes them extremely attractive for electronic industry [25].

Based on this variety of crystal structures and therewith associated broad spectrum of properties it is of utmost importance to understand the relation between deposition technique used and the attainable microstructure. Otherwise, one will not be able to grow Ta-N coatings featuring properties specifically tailored to meet the requirements of application. In this work we compare the structural evolution and mechanical properties of HiPIMS, pulsed DC and DC sputtered Ta-N films, primarily as a function of the N_2-to-total pressure ratio.

II. EXPERIMENTAL

Tantalum nitride thin films were deposited using a modified Leybold Heraeus A400-VL unbalanced magnetron sputtering system. The powder metallurgically produced Ta target (Plansee SE, 99.9% purity, $ø75x7mm^2$) was positioned 55 mm below the parallel facing substrate holder. Prior to the deposition process, austenitic (20x7x0.5 mm^3) substrates were ultrasonically cleaned in acetone and ethanol for 10 minutes. Subsequent to the heating procedure to $\approx 500\,°C$ (30 minutes holding time) the substrates were sputter-etched for 5 minutes in pure argon atmosphere. After a base pressure of approximately 0.3 Pa was reached, a metallic Tantalum interlayer of $\approx$ 100 nm thickness was deposited to ensure enhanced adhesion of the Ta-N top layers.

Argon and Nitrogen were flow-controlled injected into the chamber resulting in an N_2-to-total pressure ratio (p_{N2}/p_T) of $0, 13.4, 25.7, 38.1, 50.5, 62.9, 75.3, 87.6$, and 100%, which results in a total process pressure of $\approx$ 0.3 Pa for DC (minimum $160\,W = 3.62\,W/cm^2$, maximum $273\,W = 6.2\,W/cm^2$) and DC pulsed (duration cycle of 50 kHz, on-time for 2656 ns, minimum $139\,W = 3.2\,W/cm^2$, maximum $284\,W = 6.4\,W/cm^2$) sputtering. The cathode was operated in constant current mode ($I = 0.5\,A$) for 60 minutes. Substrates were additionally biased with $-50\,V$ to enhance growth kinetics. Due to stability reasons the working pressure for the HiPIMS process was set to approximately 0.6 Pa, and operated in constant power mode ($P = 500\,W$) and a duration cycle of 500 Hz with an on-time for 100 s, resulting in $11.3\,W/cm^2$.

The crystallographic structure of the Ta and Ta-N coatings was examined by X-ray diffraction in Grazing Incidence (GI, angle of incidence 2 deg) and Bragg-Brentano (BB, $15-90$ deg) arrangement. The Empyrean PANalytical (Θ-Θ Diffractometer) with a Cu ($K\alpha$) radiation source was additionally equipped with a monochromator and Göbel Mirror calibrated for thin film characterization. Fracture cross-sectional micrographs were acquired using a FEI Quanta 200 FEG scanning electron microscope (SEM) with an acceleration voltage of 5 keV. Analysis of the chemical composition was conducted by energy dispersive X-ray spectroscopy (EDS) with an acceleration voltage of 20 keV. However, it has to be pointed out, that chemical evaluation of heavy (Ta) and light (N) elements are extremely difficult, in this specific case most likely leading to an overestimation of Ta and consequently underestimation of N. The supplementary measurement of a selected coating by Elastic Recoil Detection Analysis points towards an error of about 12 at.%. Hardness measurements were conducted on an IBIS nanoindentation system by Fischer-Cripps Laboratories equipped with a Berkovich diamond tip. Loads from 30 to 2 mN, depending on the film thickness and surface appearance, were applied. Load displacement curves were evaluated according to Oliver and Pharr [39]. Special care was taken not to experience substrate influence.

III. RESULTS AND DISCUSSION

A. DC Sputtered Films

Fracture cross-sectional micrographs of DC sputtered Ta-N films, Fig. 1, clearly demonstrate the dependence of the developing microstructure and growth rate on the N_2-to-total pressure ratio used. The thin bright layer at the substrate interface is a metallic Ta interlayer to enhance adhesion. In pure Ar atmosphere (Fig. 1a) fine and short columns, branched into broader and longer columns, are visible. Such distinct open columnar growth usually exhibits reduced mechanical properties. On one hand the cohesion between grains with wide and large boundaries is significantly reduced, on the other hand, voids and open grain boundaries represent ideal diffusion pathways for diffusion.

The regulation to a p_{N2}/p_T-ratio of 13.4% (Fig. 1b), results in a finer-grained and dense structure with a smooth surface. The transition from a fine to coarse morphology is gradual along the whole coating thickness. The growth rate is, also due to target poisoning, reduced as compared with the pure metallic film.

The coating processed with 38.1% p_{N2}/p_T-ratio, see Fig. 1c, exhibits a similar microstructure with initially fine and subsequent larger grains. However, a more pronounced coarsening with increasing film thickness is obtained. This trend continues with higher N_2-to-total pressure ratios. The zone, which exhibits a rather rough microstructure, appears earlier in the deposition process (hence, already at lower coating thicknesses) as compared with lower nitrogen contents. This finding could be a result of the reduced deposition rate with higher N_2 partial pressure and the thereby increased time for adatoms to migrate at the film surface. Images of Ta-N coatings prepared with a N_2-to-total pressure ratio of more than 38.1% show outbursts of open columns in the cross-section, which is an indication for weakened interfaces to

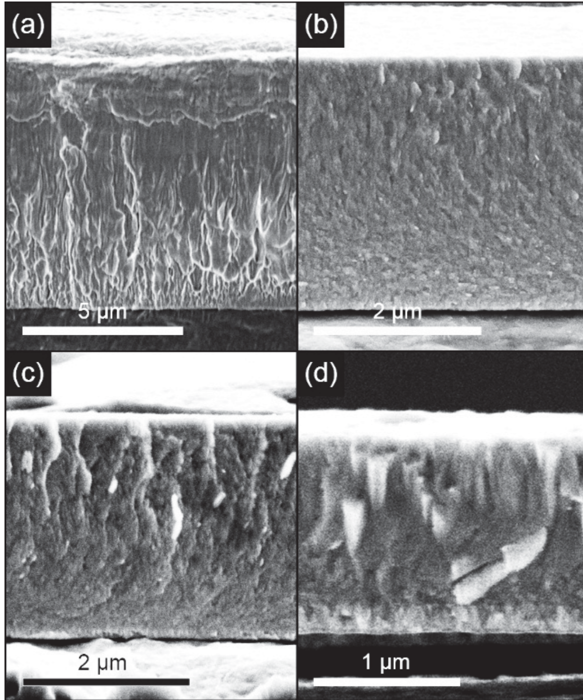

FIG. 1. Cross-sectional SEM images of DC sputtered Ta-N films. The N_2-to-total pressure ratio is increased from (a) 0 to (b) 13.4, to (c) 38.1, to (d) 75.3%.

the surrounding grains. The cross-section SEM micrograph, Fig. 1d, features detached crystallites, appearing with bright contrast.

For almost all coatings we observe partial spallation during cracking of the austenitic substrates (for the preparation of the cross-section micrographs), despite the Ta bonding layer. Cracking of the film leads to a flake-like appearance of the surface, especially for coatings prepared with p_{N2}/p_T-ratios above 50.5%.

Figure 2 shows XRD scans of reactively DC sputtered Ta-N films as a function of the N_2-to-total pressure ratio. In pure argon atmosphere (black XRD scan at the bottom), body-centered cubic α-Ta (lower half-filled blue squares, JCPDS card 00-004-0788) is formed [33, 40]. Stable α-Ta usually crystallizes at deposition temperatures above 400 °C, whereas a mixture of the stable α phase and metastable tetragonal β-Ta forms between 300 to 400 °C [41, 42]. A further decrease of deposition temperature results in the growth of films entirely composed of β-Ta (indicated by black triangles, JCPDS card 00-025-1280). In the present case, we find small portions of β-Ta as suggested by a minor XRD peak at $2\Theta = 34.5$ deg. Process induced defect densities and residual stresses of the coatings can be the reason for the observed XRD peak shift, when compared with JCPDS reference peak positions.

Upon the introduction of nitrogen gas with p_{N2}/p_T-ratio of 13.4% to the deposition chamber, at least two Ta-rich phases crystallize: orthorhombic o-Ta_4N (pink diamonds, JCPDS card 00-032-1282) and hcp γ-Ta_2N (upper half-filled green hexagons, JCPDS card 00-026-0985). The formation of o-Ta_4N and γ-Ta_2N very well corresponds with the nitrogen content within the films, suggesting for Ta-rich Ta-N phases. Peak broadening, as it is for example visible at $2\Theta \approx 73$ and ≈ 83 deg, is a result of finer coherent scattering domain sizes as well as the superposition of two or more XRD peaks.

For a p_{N2}/p_T-ratio of 25.7% a significant modification of the XRD pattern can be detected. The double peak at $2\Theta \approx 33$ and 35 deg (mainly comprising o-Ta_4N with small contributions of γ-Ta_2N) narrows and a pronounced XRD peak at 33.97 deg, a position indicative for the (100) lattice planes of γ-Ta_2N, develops. The peak asymmetry towards the right hand side is a result of superimposed (002) and (101) reflections. The previously dominant (111) o-Ta_4N XRD peak at $2\Theta \approx 37.7$ deg can not be detected anymore. On the other hand, we now can identify a cubic δ-TaN phase (indicated by upper-half filled blue squares, JCPDS card 00-032-1283) by small XRD peaks emerging at $2\Theta \approx 41.5, 60.5,$ and 72 deg.

DC sputtered Ta-N films with $p_{N2}/p_T = 38.1\%$ consist

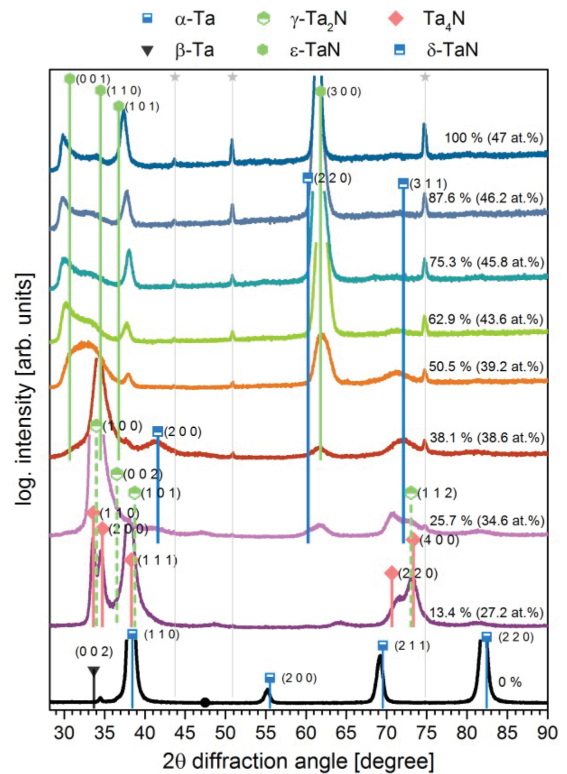

FIG. 2. XRD patterns of reactively prepared DC sputtered Ta-N films. The N_2-to-total pressure ratio is increased from 0 to 13.4, 25.7, 38.1, 50.5, 62.9, 75.3, 87.6, and 100 %.

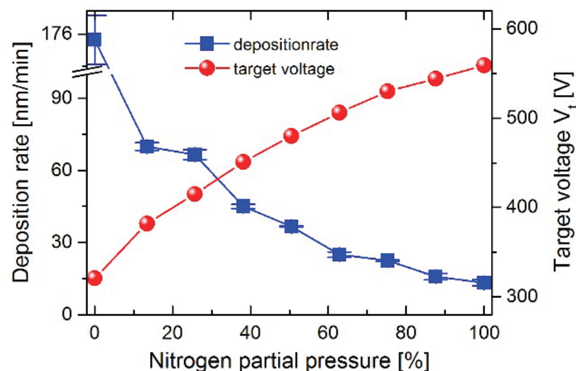

FIG. 3. Deposition rate (blue squares) and target voltage (red spheres) of DC sputtered Ta-N coatings as a function of the N_2-to-total pressure ratio.

of stoichiometric cubic δ- and hcp ϵ-TaN (green hexagons, JCPDS card 04-003-1766). The latter phase is identified by the slight XRD shoulder formation at $2\Theta \approx 32$ deg as well as emerging XRD peaks at $34.5, 36.0$ deg, and ≈ 61 deg. Even though the observed peak positions also match with N-rich Ta-N phases, we conclude, that, based on the actual nitrogen content within the coating (<50 at.%, considering the limits and errors in measurements of heavy and light elements), a defected and partially distorted stoichiometric film composition (i.e. δ- and ϵ-TaN) is more likely.

At p_{N2}/p_T-values of 50.5% and beyond, only marginal changes in the respective XRD patterns can be detected. Primarily, the δ-TaN phase decreases in intensity, whereas the respective ϵ-TaN XRD peaks intensify and sharpen, as for example seen in the 2Θ range between 30 and 33 deg. However, we have to point out that with decreasing film thickness (due to an increasing N_2-partial pressure), the metallic Ta bond layer, deposited to improve adhesion, now becomes more and more visible, see the sharp (110) XRD peak at ≈ 38.5 deg. DC sputtering of Ta targets in pure nitrogen allows for the growth of almost single-phased ϵ-TaN films. The chemical composition of these coatings, exhibiting ≈ 47 at.% nitrogen, again confirm our previous assumption of stoichiometric Ta-N phases being most likely present.

Figure 3 shows the actual target voltage, V_t (red spheres), applied during the DC sputter process. In pure argon atmosphere, V_t starts with 321 V and gradually (but non-linearly) increases up to a maximum of 559 V. Simultaneously the deposition rate (blue squares) decreases from 176 ± 11 nm/min to approximately 15 ± 3 nm/min.

This behavior can be explained by the effect of target poisoning and has intensively been investigated in the past [43, 44]. With an increasing amount of reactive gas within the chamber, a Ta-N compound layer is formed on the target surface. On one hand the resistance is increased, which in turn leads to a voltage increase (R≈U). On the other hand, the sputter efficiency is significantly reduced due to the higher cohesive energy of the nitride layer on the Ta cathode. Consequently, the continual decrease in growth rate due to the increasing nitrogen partial pressure can be explicated by the modification from metal to nitride sputtering mode [21, 45, 46].

The nanoindentation hardness H and Youngs modulus E of DC prepared coatings, as a function of the nitrogen content within the coatings measured by EDS, is presented in Figs. 4a and 4b, respectively. The hardness for metallic Ta films is about 7.7 ± 0.5 GPa, corresponding to other results showing that metallic films are typically lower in hardness than their respective nitride compounds [47]. The addition of selected elements, e.g. nitrogen, leads to a hardness increase to the range between ≈ 20 and ≈ 40 GPa [48]. The highest hardness of $H = 40 \pm 3.8$ GPa is obtained for coatings with nitrogen contents <30 at.% [21] and the corresponding Youngs modulus is approximately 380 GPa. Respective Ta-N coatings feature a dense microstructure and consist, according to previously discussed XRD results, primarily of γ-Ta_2N (with traces of o-Ta_4N). Coatings comprising a higher nitrogen concentration show a slight decrease in hardness to ≈ 25 GPa, whereas E increases to

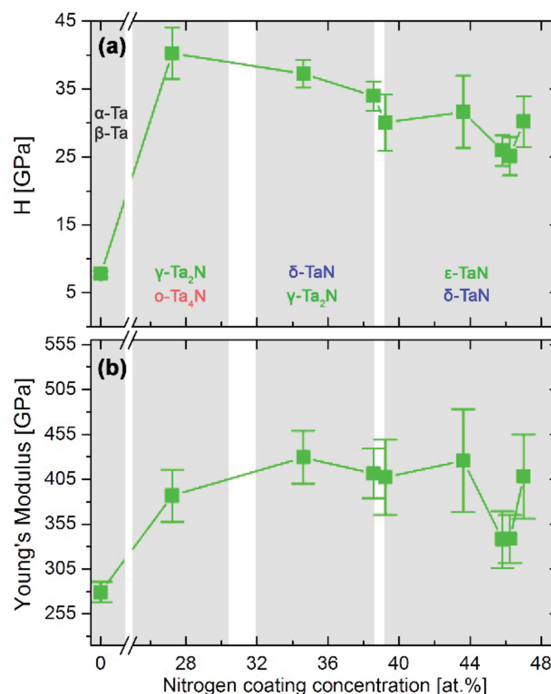

FIG. 4. (a) Hardness and (b) Youngs modulus of Ta-N coatings prepared by DC sputtering as a function of the nitrogen concentration within the coatings measured by EDS. The different Ta-N phases present in the respective nitrogen regime are indicated.

about 430 GPa. The hardness drop can on one hand be explained by the developing columnar microstructure (please see Fig. 1d), and on the other hand by the presence of hcp ϵ-TaN. Furthermore, the reduced film thickness (constant deposition time for all coatings, but decreasing growth rates due to target poisoning) may also influence the hardness values, although special attention was paid to reduce substrate interference during nanoindentation. Above $p_{N2}/p_T = 62.9\,\%$ a steep decrease of Youngs modulus to values of 330 GPa is observed, followed by an increase to 405 GPa. This actually suggests that the coatings prepared with $p_{N2}/p_T = 75.3$ and 87.6% contain a higher phase fraction of ϵ-TaN (therefore, significantly lower Youngs modulus and hardness) than the coating prepared with $p_{N2}/p_T = 100\%$. This would actually agree with the XRD results showing that the pronounced XRD peak at 62 deg diffraction angle is shifted towards δ-TaN when using a p_{N2}/p_T ratio of 100 %.

B. Pulsed DC Sputtered Films

Fracture cross-sectional micrographs of pulsed DC sputtered Ta-N films are provided in Fig. 5.

In pure Ar atmosphere (Fig. 5a) a distinct open columnar morphology is visible, which upon increasing N_2-to-total pressure ratio to 13.4 % (Fig. 5b), evolves into a finer-grained, hence more compact, microstructure. The respective coating cross-section for the DC prepared Ta-N films (see Fig. 1b) does not exhibit such a fine and dense structure. This suggests, that film growth is effectively enhanced by the use of a pulsed DC system. Higher p_{N2}/p_T-values result in the development of an amorphous-like layer at the interface to the Ta-adhesion layer, followed by a fine-grained structure. This is especially pronounced for the coating prepared with p_{N2}/p_T = 25.7 and 38.1 % (Fig. 5c). Figure 5d shows the cross-section of the coating prepared with $p_{N2}/p_T = 75.3\,\%$, which can be seen as a representative for all coatings prepared with p_{N2}/p_T-values above 40 %. The dual character of an initially fine amorphous-like structure followed by evolving grains is typical for these coatings. Similar to DC prepared coatings, we can identify distinct crystallites appearing bright in the respective cross-section micrographs.

Figure 6 shows Bragg-Brentano XRD patterns of Ta-N films prepared by pulsed DC sputtering as a function of the N_2-to-total pressure ratio.

In pure argon atmosphere, body-centered cubic α-Ta is formed, which, compared to DC grown Ta films, exhibits

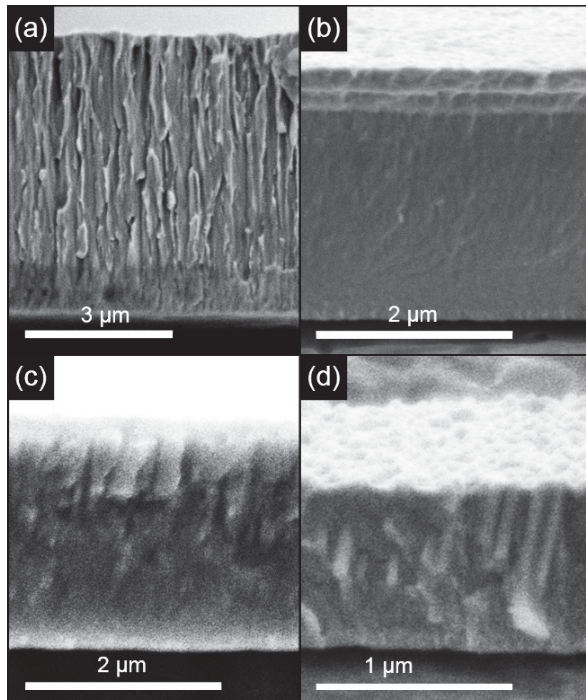

FIG. 5. Cross-sectional SEM images of pulsed DC sputtered Ta-N films. The N_2-to-total pressure ratio is increased from 0 (a) to 13.4 (b), 38.1 (c), to 75.3% (d).

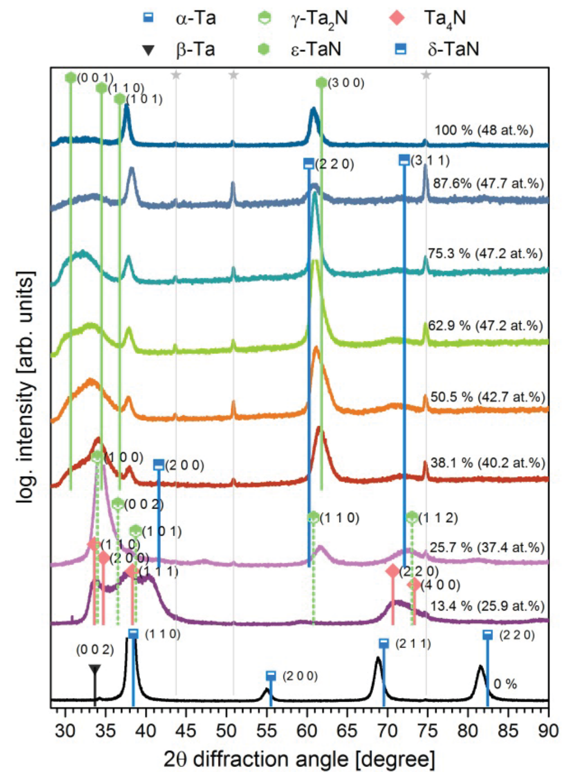

FIG. 6. Bragg-Brentano XRD patterns of pulsed DC sputtered Ta-N films. The N_2-to-total pressure ratio is increased from 0 to 13.4, 25.7, 38.1, 50.5, 62.9, 75.3, 87.6, and 100%.

XRD peak positions slightly shifted to lower diffraction angles. Again, we can identify β-Ta by a weak XRD peak at $2\Theta = 34.5$ deg. Upon the introduction of nitrogen, $p_{N2}/p_T = 13.4\%$, o-Ta_4N and γ-Ta_2N crystallize, yet with broader peaks and reduced intensity. The broadening suggests finer coherent-scattering crystallite sizes as compared with the DC sputtered counterparts. By pulsing the DC current, one aims for enhanced ion bombardment, which in turn hinders the development of large columns [46]. The broad asymmetric XRD peak between $2\Theta = 70$ and 75 deg clearly demonstrates the (at least) dual-phased constitution of the films. Corresponding to the results shown in Fig. 2 for DC sputtered films, a p_{N2}/p_T-value of 38.1% results in the formation of stoichiometric δ- and ϵ-TaN phases. Nonetheless, deviations from the JCPDS reference peak positions suggest partially distorted and (most likely) highly defected structures. The major XRD peaks can all be assigned to the hcp ϵ-TaN phase, whereas the slight broadening at ≈ 72 deg still suggests small phase fractions of cubic δ-TaN. The crystallographic modifications upon further increasing the nitrogen partial pressure is rather marginal, again similar to DC sputtered films, pointing towards a continuous development of ϵ-TaN structured coatings at the expanse of δ-TaN. At 100% nitrogen (i.e. ≈ 48 at.% N within the coatings) we assume that ϵ-TaN is the dominating phase present. Again, the (110) XRD peak of the metallic Ta bond layer becomes continuously stronger in intensity, because the coating thickness decreases.

Deposition rate and target voltage, V_t, as a function of the N_2-to-total pressure ratio is shown in Fig. 7. Both parameters are lower as compared with DC prepared coatings, however the general trend is similar. The deposition rate exhibits a peak value of 81 ± 3 nm/min at 0% N_2. A plateau develops between p_{N2}/p_T-ratios of 13.4 and 38.1%, extending to higher N_2-to-total pressure ratios than seen for the DC coatings (Fig. 3). A further increase of the nitrogen content leads to an almost linear decrease in deposition rate [49]. Interestingly, the final value of the deposition rate, at 100% nitrogen partial pressure, again increases to 13.4 ± 4 nm/min, and is rather similar to that of DC sputtering.

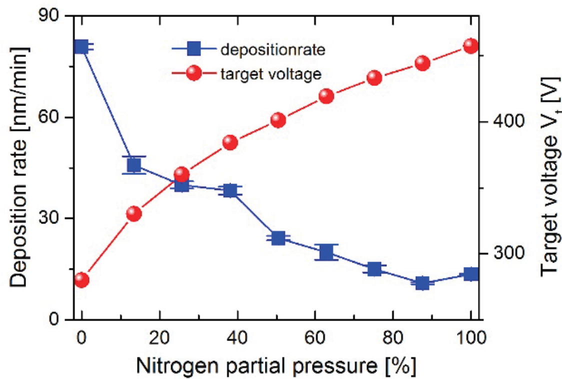

FIG. 7. Deposition rate (blue squares) and target voltage (red spheres) of Ta-N coatings as a function of the N_2-to-total pressure ratio used during pulsed DC sputtering.

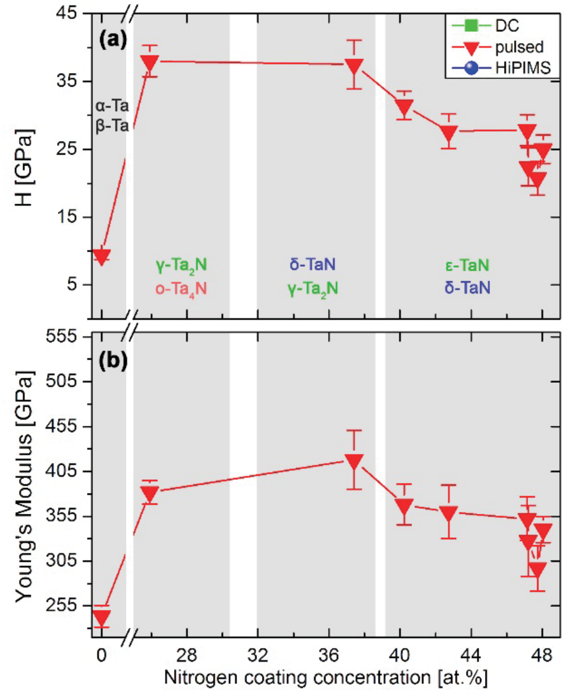

FIG. 8. (a) Hardness and (b) Youngs Modulus of Ta-N coatings prepared by pulsed DC sputtering as a function of the nitrogen concentration within the coatings measured by EDS. The different Ta-N phases present for the respective nitrogen regime are indicated.

Figures 8a and b show the nanoindentation hardness H and Youngs modulus of pulsed DC prepared coatings as a function of their nitrogen content. The hardness of Ta processed in pure Ar atmosphere is about 9.4 ± 0.5 GPa. In contrast to DC sputtering, a smoother cross-sectional microstructure is obtained, which can be attributed to the higher momentum transfer during pulsed DC sputtering [46].

In the present study, the highest hardness of $H = 38 \pm 4.5$ GPa is obtained for the coating containing 25.9 at.% nitrogen, in good agreement with Valleti et al. [46]. The corresponding Youngs modulus is about 375 GPa. A further increase of p_{N2}, thus increases in nitrogen coating concentration, does not significantly influence the hardness, although the Youngs modulus is increased to approximately 400 GPa. Higher nitrogen partial pressures lead to a continuous reduction of γ-Ta_2N phase fraction and an increase in δ- and particularly ϵ-TaN phase fraction. This in turn leads to a decrease in hardness and Youngs moduli to around 25 GPa and 310 GPa, respectively.

C. HiPIMS Films

Typical examples of fracture cross-sectional SEM images of HiPIMS Ta-N coatings deposited with varying N_2 partial pressures are provided in Fig. 9. The initial morphology of the metallic Ta layer, features a more distinct open columnar appearance, see Fig. 9a, as compared to the DC film. At $p_{N2}/p_T = 13.4\%$ (Fig. 9b) the microstructure changes from columnar to tightly packed fine-fibrous grains. The growth rate, due to target poisoning, decreases. A further grain refinement occurs for a further increase in p_{N2}/p_T to 25.7%. Contrary to the DC sputter process, coatings prepared with p_{N2}/p_T-ratios of 38.1 (Fig. 9c) and 50.5% exhibit a significantly finer-grained, hence more compact, microstructure. Actually the coatings are more comparable to the cross-section presented in Fig. 1d, which actually represents a DC sputtered coating prepared with $p_{N2}/p_T = 75.3\%$. With p_{N2}/p_T-values between 62.9 and 75.3% (Fig. 9d) the coatings exhibit a fine amorphous-like growth morphology close to the substrate (or the Ta bond layer) and a more coarse grained growth morphology closer to the surface region. This is very similar to the growth morphology of DC and pulsed DC sputtered Ta-N coatings prepared at very high nitrogen partial pressures. In agreement with the XRD investigations, this points towards a mainly single-phase growth morphology of our coatings. Based on these results we conclude, that HiPIMS allows for a similar growth morphology and microstructures as DC and pulsed DC sputtering, but already at lower nitrogen partial pressures. Further increasing the p_{N2}/p_T to 87.6 and 100% results in serve arcing on the target during the HiPIMS mode, which is why such coatings were not grown.

Figure 10 shows Bragg-Brentano XRD patterns of Ta-N films prepared by HiPIMS. The crystallographic composition of the coatings prepared in pure argon atmosphere is comparable to pulsed DC and DC sputtered coatings. Although, the HiPIMS coatings exhibit a pronounced (100) and (220) growth orientation.

With a N_2-to-total pressure ratio of 13.4%, the coatings are nearly γ-Ta_2N single-phase structured with a pronounced (100) growth orientation. The DC and pulsed DC sputtered films still contained metallic Ta and o-Ta_4N phases next to γ-Ta_2N for $p_{N2}/p_T = 13.4\%$, please compare Fig. 2 and Fig. 6, respectively. SEM EDS measurements clearly show, that the HiPIMS coatings prepared with $p_{N2}/p_T = 13.4\%$ already contain about 38.6 at.% N, in agreement with the observed γ-Ta_2N structure.

With a further increase in p_{N2}/p_T to 25.7%, cubic δ-

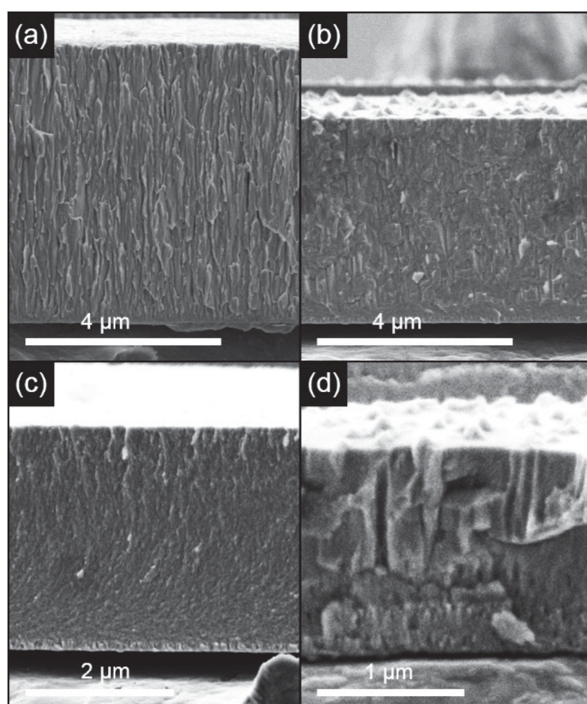

FIG. 9. Cross-sectional SEM images of Ta-N films grown by HiPIMS with varying N_2-to-total pressure ratio of (a) 0, (b) 13.4, (c) 38.1, and (d) 75.3%.

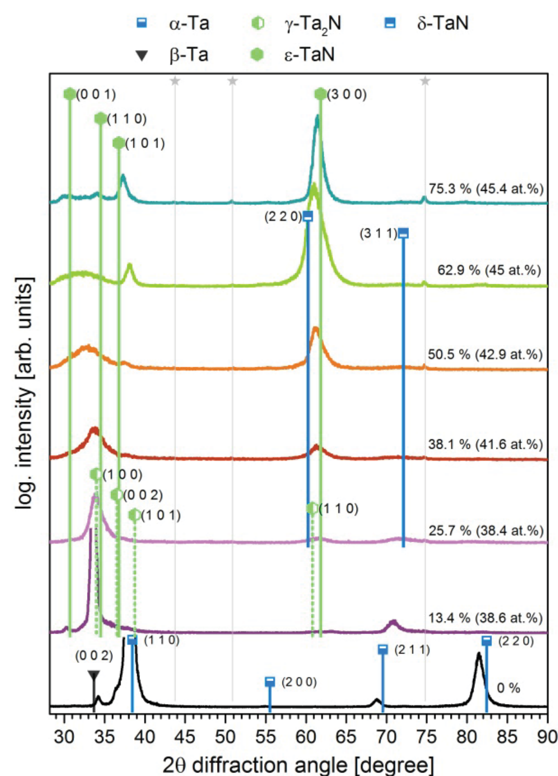

FIG. 10. Bragg-Brentano XRD patterns of reactively prepared HiPIMS Ta-N films. The N_2-to-total pressure ratio increases from 0 to 13.4, 25.7, 38.1, 50.5, 62.9, to 75.3%.

TaN is formed, see the low-intensity and broadened XRD peak at $2\Theta \approx 62$ deg. For this coating it is difficult to identify whether the XRD peak at around 34 deg stems from γ-Ta_2N or ϵ-TaN. The nitrogen content suggests for a γ-Ta_2N phase. Upon further increasing p_{N2}/p_T, the ϵ-TaN or δ-TaN phase fraction increases. If we concentrate our interpretation on the XRD peak at around 60 deg, the XRD data suggest that first the δ-TaN phase fraction increases (until $p_{N2}/p_T = 62.9\%$) and than upon further increasing p_{N2}/p_T to 75.3%, the ϵ-TaN phase is dominating. This interpretation is based on the shift of this XRD peak (at around 60 deg) towards smaller diffraction angles for increasing p_{N2}/p_T to 62.9% and than to higher diffraction angles when increasing p_{N2}/p_T to 75.3%. Consequently, the coating prepared at p_{N2}/p_T = 75.3% exhibits nearly a single-phased ϵ-TaN structure. This coating contains around 45.5 at.% nitrogen, as suggested by EDS.

The deposition rate and target voltage, V_t, as a function of the N_2-to-total pressure ratio is presented in Fig. 11. The deposition rates of the coatings prepared by HiPIMS are rather comparable to their DC sputtered counterparts, in value and dependence on the nitrogen partial pressure. The voltage is significantly higher as compared to DC and pulsed DC sputtering. We envision (and that is content of further investigation) that the nearly similar deposition rates between DC sputtering and HiPIMS is based on the significantly higher total pressure of 0.6 Pa during HiPIMS as compared to the 0.3 Pa during DC sputtering.

However, the similar deposition rates between DC sputtering and HiPIMS allows comparing the phase formation sequence as a function of nitrogen partial pressure. HiPIMS allows to grow γ-Ta_2N dominated films with lower nitrogen-to-total pressure ratios than DC sputtering. As the deposition rate for HiPIMS is similar to that of DC sputtering (for comparable nitrogen-to-total pressure rations) the higher reactivity of the species

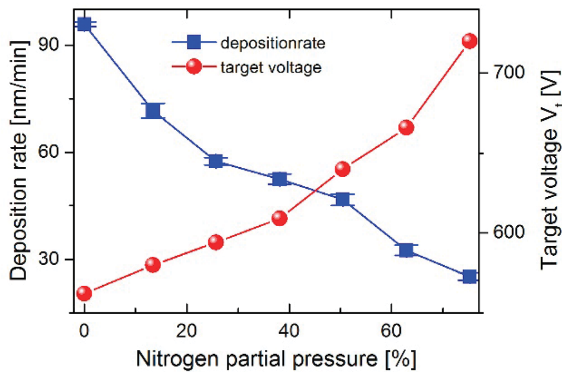

FIG. 11. Deposition rate (blue squares) and target voltage (red spheres) of HiPIMS Ta-N coatings as a function of the N_2-to-total pressure ratio.

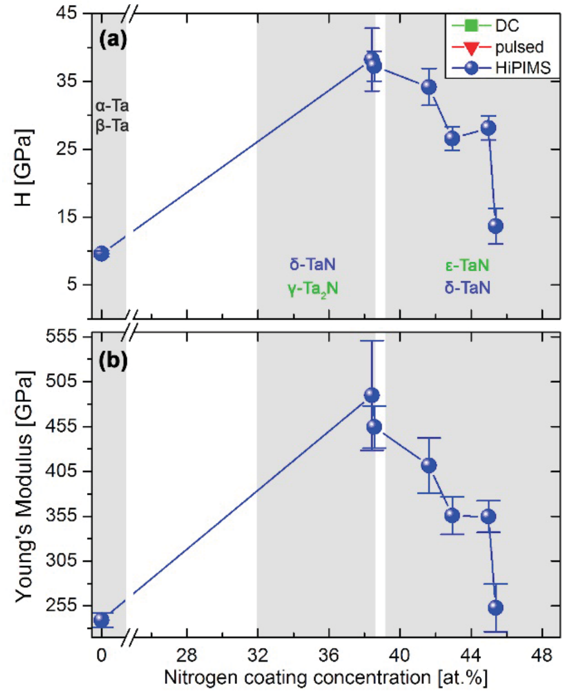

FIG. 12. (a) Hardness and (b) Youngs modulus of Ta-N coatings prepared by HiPIMS as a function of the nitrogen concentration within the coatings measured by EDS. The different Ta-N phases present in the respective nitrogen regime are indicated.

prepared by HiPIMS is responsible for this effect and not a lower deposition rate.

Figures 12a and b represent the nanoindentation hardness and Youngs modulus of the HiPIMS Ta-N coatings as a function of p_{N2}/p_T, respectively. A hardness of 9.6 ± 0.5 GPa with a corresponding low Youngs modulus of 245 GPa is observed for metallic Ta films, prepared with $p_{N2}/p_T = 0\%$.

At N_2-to-total pressure ratios of 13.4 and 25.7% the coatings exhibit increased hardness of approximately 37.8 GPa. Similarly, the Youngs modulus increases to almost 500 GPa. The dominant phases present in these coatings are γ-Ta_2N and δ-TaN. For higher nitrogen contents (up to around 44 at.%) the hardness and Youngs modulus decreases, due to the developing δ- and ϵ-TaN phases. The coating prepared with the highest p_{N2}/p_T ratio of 75.3% exhibits a significantly lower hardness and Youngs modulus than the coating prepared with p_{N2}/p_T = 62.9%, although having a rather similar nitrogen content of ≈ 45 at.%. This again supports our interpretation of the XRD results of a dominating δ-TaN structure for $p_{N2}/p_T = 62.9\%$ but a dominating ϵ-TaN structure for $p_{N2}/p_T = 75.3\%$, because both coatings exhibit a rather similar nitrogen content and deposition rate. Hence, the slightly different film thickness should not play such a sig-

nificant role to explain this sudden drop in hardness from $H = 26$ to 12 GPa, which is also reflected by the drop in Youngs modulus. But a connected sudden change in dominating growth structure can explain this behavior.

D. Discussion

Tantalum nitride thin films were deposited on austenitic substrates by HiPIMS, pulsed DC and DC sputtering with varying N_2-to-total pressure ratios from 0 to 100%, and compared in terms of microstructure and phase evolution, and mechanical properties. The comparison of growth rates, provided in Fig. 13, clearly demonstrates that DC allows for high growth rates of approximately 175 ± 5 nm/min for $p_{N2}/p_T = 0\%$. Pulsed DC sputtering and HiPIMS lead to Ta growth rates of 80 to 85 nm/min (for $p_{N2}/p_T = 0\%$). With the addition of nitrogen, the growth rates for DC sputtering and HiPIMS a rather similar in value and dependence on p_{N2}/p_T. Here, we have to mention, that due to the instability of the HiPIMS process for $p_T = 0.3$ Pa we needed to increase p_T to 0.6 Pa, whereas for DC and pulsed DC sputtering the total pressure p_T was 0.3 Pa. As often observed, the pulsed DC sputtering and HiPIMS technique show a slightly lower decline in deposition rate with increasing p_{N2}/p_T than DC sputtering, Fig. 13.

Within the three investigated sputtering techniques, HiPIMS is most efficient to introduce nitrogen into the coatings, Fig. 14. Already for the rather low p_{N2}/p_T-ratio of 13.4% the HiPIMS coatings contain about 38.5 at.% nitrogen, whereas the DC and pulsed DC sputtered coatings exhibit only 26.5 at%. For higher p_{N2}/p_T-values, the nitrogen contents are rather similar for the individually prepared coatings. For p_{N2}/p_T-ratios above approximately 60%, the nitrogen seems to have reached a steady state concentration of about 45 at.%.

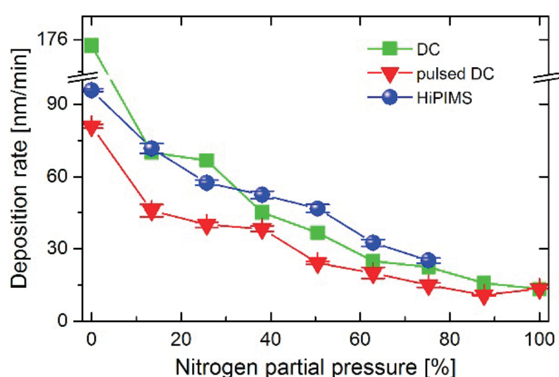

FIG. 13. Deposition rate of Ta-N coatings as a function of the N_2-to-total pressure ratio used during DC sputtering (green squares), pulsed DC sputtering (red triangles), and HiPIMS (blue spheres).

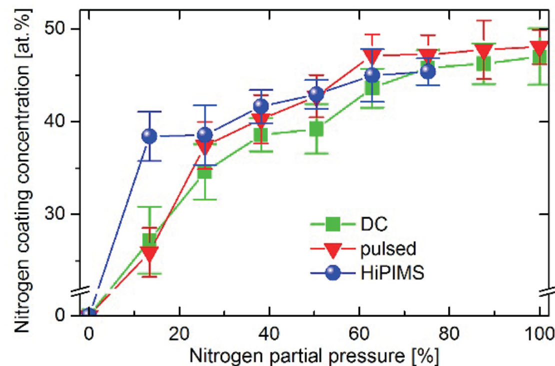

FIG. 14. Nitrogen concentration of Ta-N thin films as a function of the N_2-to-total pressure ratio used during DC sputtering (green squares), pulsed DC sputtering (red triangles), and HiPIMS (blue spheres).

Nanoindentation measurements for metallic tantalum films indicate hardness values in the range of $8-10$ GPa for all sputtering techniques investigated, see Fig. 15. Tantalum coatings sputtered in pure argon atmosphere form a stable cubic α-Ta phase with an (110) growth orientation, featuring a pronounced open columnar morphology. Minor phase fractions of β-Ta can be detected, with the smallest intensity for the HiPIMS coatings.

Upon the addition of nitrogen, o-Ta_4N and γ-Ta_2N (only γ-Ta_2N for HiPIMS Ta-N) phases are formed. Coatings primarily consisting of γ-Ta_2N phases (with only a small fraction of o-Ta_4N for the pulsed DC and DC sputtered films) outperform all other coatings investigated in terms of mechanical properties. Their hardness is about 40 GPa, which is obtained for the DC and pulsed DC sputtered coatings containing ≈ 26.5 at.% N and the HiPIMS coatings containing ≈ 38.5 at.% N. The Youngs moduli of the HiPIMS coatings are significantly higher ($\approx$ 470 GPa) than their DC and pulsed DC sputtered counterparts. We attribute this to the nearly γ-Ta_2N phase-pure structure of the HiPIMS coating, whereas the DC and pulsed DC sputtered coatings contain also a minor phase fraction of o-Ta_4N.

A further increase of the N_2-to-total pressure ratio to values beyond 38.1% leads to structural modifications from primarily Ta-rich to stoichiometric cubic δ-TaN and hcp ϵ-TaN phases. As a consequence, the hardness and Youngs moduli decrease. Whereas most of these coatings, prepared by pulsed DC and DC sputtering or HiPIMS, exhibit comparable hardness and Youngs moduli (within the error of measurement), one HiPIMS coating is out of the general behaviour. This coating is prepared at the highest N_2-to-total pressure ratio of 75.3% possible during HiPIMS and exhibits the lowest hardness for the Ta-N coatings with only 14 GPa. Also the corresponding Youngs modulus is lowest with only $\approx$ 255 GPa. This coating is not significantly thinner as the other ones, but

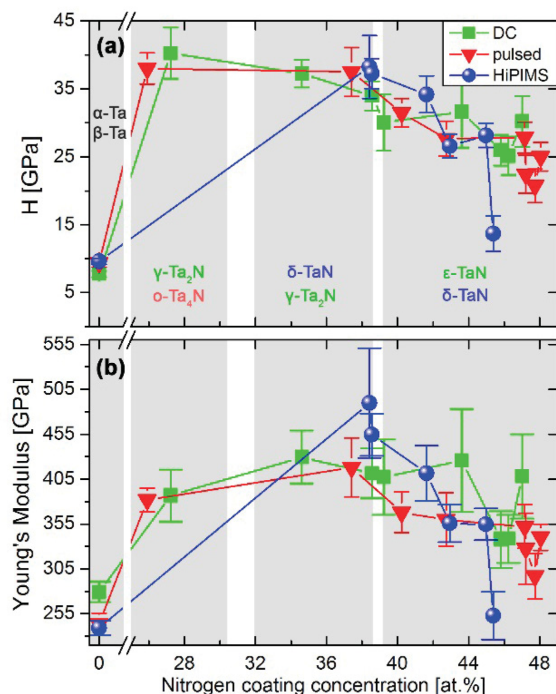

FIG. 15. (a) Hardness and (b) Youngs modulus of Ta-N coatings as a function of their nitrogen concentration prepared by DC sputtering (green squares), pulsed DC sputtering (red triangles), and HiPIMS (blue spheres). The different Ta-N phases present in the respective nitrogen regime are indicated.

the XRD data suggest that here the ϵ-TaN phase is dominating. As the DC sputtered coating—using a N_2-to-total pressure ratio of 100%—shows a rather high hardness ($H \approx 27$ GPa) and Youngs modulus ($E \approx 400$ GPa) and their XRD data suggest for a dominating δ-TaN, we envision that the ratio between ϵ-TaN and δ-TaN phases dominates the hardness and Youngs modulus of these Ta-N coatings with nitrogen contents between 40 and 48 at.%.

IV. CONCLUSIONS

Tantalum nitride thin films grown by DC and pulsed DC sputtering as well as HiPIMS were compared with each other in terms of microstructure, phase evolution, resulting mechanical properties and their dependence on the used nitrogen-to-total pressure ratio (i.e. p_{N2}/p_T).

In pure Argon atmosphere ($p_{N2}/p_T = 0$ %) all coatings (DC and pulsed DC sputtered and HiPIMS) exhibit body-centered cubic α-Ta with small fractions of tetragonal β-Ta. Increasing p_{N2}/p_T to 13.4 % leads to the formation of hcp γ-Ta_2N with a small fraction of orthorhombic o-Ta_4N for DC and pulsed DC sputtered coatings, exhibiting ≈ 26.5 at.% N. Their HiPIMS counterpart already contains 38.5 at.% N for this nitrogen-to-total pressure ratio and exhibits a γ-Ta_2N dominating structure. These coatings exhibit the highest hardnesses with 40.0 ± 3.8 GPa (DC), 38.2 ± 4.6 GPa (pulsed DC), and 38.0 ± 2.3 GPa (HiPIMS), respectively, among all coatings investigated. Upon a further increase in p_{N2}/p_T to 25.7 %, the DC and pulsed DC sputtered films contain 34.6 and 37.4 at.% N, respectively, and their structure is now dominated by γ-Ta_2N with small fractions of δ-TaN. Their HiPIMS counterpart also, still contains a dominating γ-Ta_2N structure (now, with small fractions of δ-TaN) and about 38.5 at.% N. The coatings, which exhibit a γ-Ta_2N dominated structure, have also the highest Youngs moduli with around 430, 400 and 500 GPa for the coatings prepared by DC sputtering, pulsed DC sputtering, and HiPIMS, respectively. First indications of ϵ-TaN phases can be detected for the coatings prepared with a p_{N2}/p_T-ratio of 38.1 %. Here, the nitrogen contents of the DC sputtered, pulsed DC sputtered and HiPIMS coatings are 38.6, 40.2, and 41.6 at.%. Upon further increasing the p_{N2}/p_T-ratio, the nitrogen content within the coatings does not increase that significantly, and is between 45 and 48 at.% for $p_{N2}/p_T \geq 62.9$ % (or 75.3 % when using DC sputtering). However, their hardness and Youngs modulus decreases and XRD data suggest that this is mainly caused by the increasing phase-fraction of ϵ-TaN on the expanse of δ-TaN. This is further supported by the HiPIMS coating prepared with $p_{N2}/p_T = 75.3$ %, which exhibits a nearly single-phase ϵ-TaN structure and the lowest hardness ($H = 13.6$ GPa) and Youngs modulus ($E = 250$ GPa) of all Ta-N coatings developed.

Using a total pressure p_T of 0.6 Pa during HiPIMS, which is twice that used during DC and pulsed DC sputtering, allowed us to obtain nearly the same deposition rate for HiPIMS and DC sputtered Ta-N coatings. Thereby we can conclude, that HiPIMS is more effective to introduce nitrogen into the coatings and to form nitrides than DC sputtering. Although the sequence of phases (γ-Ta_2N, δ-TaN, ϵ-TaN) is rather similar, their crystallization is obtained at lower p_{N2}/p_T-ratios when using HiPIMS instead of DC sputtering.

ACKNOWLEDGEMENTS

The authors greatly acknowledge the financial support of Plansee Composite Materials GmbH, Oerlikon Surface Solutions AG and the Christian Doppler Gesellschaft within the framework of the Christian Doppler Laboratory for Application Oriented Coating Development at the Vienna University of Technology.

[1] K. Eda, T. Miwa, Y. T. A, and I. Tomokl, IEEE Transactions of Microwave Theory and Techniques (1990).
[2] R. E. Hampy, Transactions on Parts, Hybrids, and Packaging (1975).
[3] H. Holleck, "Advanced concepts of PVD hard coatings," (1990).
[4] G. A. Patrizi, **291**, 513 (1996).
[5] K. Radhakrishnan, N. Geok Ing, and R. Gopalakrishnan, Mater. Sci. Eng. B **57**, 224 (1999).
[6] Y. Ogura, C. Kobayashi, Y. Ooba, N. Yahata, and H. Sakamoto, Surf. Coatings Technol. **200**, 3347 (2006).
[7] C. Technology, H. Holleck, and K. Karlsruhe, **44**, 245 (1990).
[8] P. H. Mayrhofer, M. Geier, C. Löcker, and L. Chen, Int. J. Mater. Res. **100**, 1052 (2009).
[9] N. D. Nam, M. Vaka, and N. Tran Hung, J. Power Sources **268**, 240 (2014).
[10] C.-H. Hsu, C.-Y. Lee, Z.-H. Lin, W.-Y. Ho, and C.-K. Lin, Thin Solid Films **519**, 4928 (2011).
[11] S. Ulrich, H. Holleck, J. Ye, H. Leiste, R. Loos, M. Stüber, P. Pesch, and S. Sattel, Thin Solid Films **437**, 164 (2003).
[12] S. Grasser, R. Daniel, and C. Mitterer, Surf. Coatings Technol. **206**, 4666 (2012).
[13] D. Holec, "private communications with David Holec, 2014, Vienna University of Technology,".
[14] K. Kutschej, P. Mayrhofer, M. Kathrein, P. Polcik, R. Tessadri, and C. Mitterer, Surf. Coatings Technol. **200**, 2358 (2005).
[15] M. Pfeiler, K. Kutschej, M. Penoy, C. Michotte, C. Mitterer, and M. Kathrein, Surf. Coatings Technol. **202**, 1050 (2007).
[16] R. Rachbauer, J. J. Gengler, A. a. Voevodin, K. Resch, and P. H. Mayrhofer, Acta Mater. **60**, 2091 (2012).
[17] D. Rafaja, C. Wüstefeld, C. Baehtz, V. Klemm, M. Dopita, M. Motylenko, C. Michotte, and M. Kathrein, Metall. Mater. Trans. A **42**, 559 (2010).
[18] C. Wüstefeld, D. Rafaja, V. Klemm, C. Michotte, and M. Kathrein, Surf. Coatings Technol. **205**, 1345 (2010).
[19] L. Gladczuk, A. Patel, J. D. Demaree, and M. Sosnowski, Thin Solid Films **476**, 295 (2005).
[20] K. Holloway and P. M. Fryer, Appl. Phys. Lett. **57**, 1736 (1990).
[21] S. Kim and B. Cha, Thin Solid Films **475**, 202 (2005).
[22] Y.-I. Chen, B.-L. Lin, Y.-C. Kuo, J.-C. Huang, L.-C. Chang, and Y.-T. Lin, Appl. Surf. Sci. **257**, 6741 (2011).
[23] K.-Y. Liu, J.-W. Lee, and F.-B. Wu, Surf. Coatings Technol. **382232** (2014), 10.1016/j.surfcoat.2014.03.024.
[24] S. Tsukimoto, M. Moriyama, and M. Murakami, Thin Solid Films **460**, 222 (2004).
[25] C. Stampfl and A. Freeman, Phys. Rev. B **71**, 024111 (2005).
[26] X. Liu, G. Ma, G. Sun, Y. Duan, and S. Liu, Appl. Surf. Sci. **258**, 1033 (2011).
[27] N. Patel, S. Wang, A. Inspektor, and P. a. Salvador, Surf. Coatings Technol. **254**, 21 (2014).
[28] J. An and Q. Zhang, Surf. Coatings Technol. **200**, 2451 (2005).
[29] D. M. Findlay, K. Welldon, G. J. Atkins, D. W. Howie, A. C. Zannettino, and D. Bobyn, Biomaterials **25**, 2215 (2004).
[30] G. Ma, G. Lin, S. Gong, X. Liu, G. Sun, and H. Wu, Vacuum **89**, 244 (2013).
[31] G. Lee, H. Kim, H. Choi, and J. Lee, Surf. Coatings Technol. **201**, 5207 (2007).
[32] N. Terao, Jpn. J. Appl. Phys. **10**, 248 (1971).
[33] C. Shin, Y. Kim, D. Gall, J. E. Greene, and I. Petrov, **402**, 172 (2002).
[34] P. H. Mayrhofer, C. Mitterer, and H. Clemens, Adv. Eng. Mater. **7**, 1071 (2005).
[35] J. Lin, J. J. Moore, W. D. Sproul, S. L. Lee, and J. Wang, IEEE Trans. Plasma Sci. **38**, 3071 (2010).
[36] A. Arakcheeva, G. Chapuis, and V. Grinevitch, Acta Crystallogr. Sect. B Struct. Sci. **58**, 1 (2001).
[37] V. F. Shamra, J. K. Warhulska, A. V. Arakcheeva, and V. V. Grinevich, **49**, 1025 (2004).
[38] C.-S. Shin, D. Gall, Y.-W. Kim, P. Desjardins, I. Petrov, J. E. Greene, M. Oden, and L. Hultman, J. Appl. Phys. **90**, 2879 (2001).
[39] W. C. Oliver and G. M. Pharr, Journal of Materials Research , 1564 (1992).
[40] T. Elangovan, S. Murugeshan, D. Mangalaraj, P. Kuppusami, S. Khan, C. Sudha, V. Ganesan, R. Divakar, and E. Mohandas, J. Alloys Compd. **509**, 6400 (2011).
[41] Y. Danon, C. Lee, C. Mulligan, and G. Vigilante, IEEE Trans. Magn. **40**, 1826 (2004).
[42] L. Gladczuk, A. Patel, C. Singh Paur, and M. Sosnowski, Thin Solid Films **467**, 150 (2004).
[43] J. Alami, K. Sarakinos, F. Uslu, and M. Wuttig, J. Phys. D. Appl. Phys. **42**, 015304 (2009).
[44] P. E. Hovsepian, A. a. Sugumaran, Y. Purandare, D. a.L. Loch, and A. P. Ehiasarian, Thin Solid Films **562**, 132 (2014).
[45] S. Noda, K. Tepsanongsuk, Y. Tsuji, Y. Kajikawa, Y. Ogawa, and H. Komiyama, J. Vac. Sci. Technol. A Vacuum, Surfaces, Film. **22**, 332 (2004).
[46] K. Valleti, J. Vac. Sci. Technol. A Vacuum, Surfaces, Film. **27**, 626 (2009).
[47] A. Cavaleiro and J. T. M. De Hosson, *Nanostructured Coatings* (2006) p. 407.
[48] J. Musil, Surf. Coatings Technol. **207**, 407 (2012).
[49] A. Aryasomayajula, K. Valleti, S. Aryasomayajula, and D. G. Bhat, Surf. Coatings Technol. **201**, 4401 (2006).